Jousset, P., Haberland, C., Bauer, K., Arnason, K. (2011): Hengill geothermal volcanic complex (Iceland) characterized by integrated geophysical observations. - Geothermics, 40, 1, 1-24

DOI: 10.1016/j.geothermics.2010.12.008

Hengill geothermal volcanic complex (Iceland) characterized by integrated geophysical observations

Philippe Jousset*[1], Christian Haberland[2], Klaus Bauer[2],

Knutur Arnason[3]

[1]BRGM – ARN, 45060 Orleans Cedex 02, France.

[2]GeoForschungsZentrum Potsdam - Section 2.2, 14473 Potsdam, Germany.

[3]Iceland GeoSurvey - ISOR , 108 Reykjavík, Iceland

Abstract

Structural features of volcanic and hydrothermal systems can be used to infer the location of magma chambers or productive geothermal areas. The Hengill volcanic triple-junction complex has a well-developed geothermal system, which is being exploited to extract hot fluids that are used for electrical power and heat production. In the framework of the I-GET project, a 4-month temporary seismological network including seven high-dynamic broadband instruments was deployed and 1D transient electromagnetic soundings (TEM) and 3D magnetotelluric (MT) surveys were performed to improve understanding of the relationships between structural features, seismic activity and fluid production at the Hengill geothermal system. The MT and TEM data set is analyzed elsewhere. The analysis of the seismological data set allowed the detection and classification of more than 600 earthquakes, among which long-period (LP) earthquakes were observed for the first time in this area. This work focuses first on a joint inversion for the 3D velocity structure and determination of the locations of the hypocentres from about 250 local volcano-tectonic earthquakes with clear P- and S- wave arrival times. The results confirm those from earlier tomography studies in this area. Integrating the seismic velocity and resistivity models in a semi-quantitative approach by cross-plotting the resistivity model with the velocity ratio V_P/V_S delineates a structural body with a high seismic velocity ratio and low resistivity that is interpreted as the main heat source of the geothermal system.

Keywords: Hengill volcano, Integrated geophysics, Broadband seismology, Seismic tomography, Resistivity, Fluids.

*Corresponding author. Tel.: +33(0)238643237 Fax.: +33(0)238643689 E-mail: p.jousset@brgm.fr

1 Introduction

Hydrothermal systems offer a low-CO_2-emission alternative energy supply (Barnea, 1972). The exploitation of geothermal energy is limited at present because drilling exploration wells is expensive and hydrothermal systems are often associated with volcanic and seismic activity (Gudmundsson and Arnórson, 2002; Stimac et al., 2003), which may put geothermal exploitation at risk (Ward, 1972; Tester et al., 2006; Majer et al., 2007). Remote characterization of reservoir properties is of significant economic importance for the geothermal industry (Ragnarsson, 2010). Knowledge of structural features of targeted geothermal systems is critical prior to drilling to reduce the dry-hole risk.

Passive seismology is one of the most cost-effective geophysical methods to infer the crustal structure of geothermal systems and volcanoes. Both the compressional P-wave velocity V_P and shear S-wave velocity V_S and V_P/V_S ratio vary with fluid composition and rock porosity and temperature. Both the classical local seismic tomography in those areas where local seismicity is high (e.g., Benz et al., 1996) and newly developed surface-wave tomography techniques applied to ambient seismic noise can image crustal subsurface structure (e.g., Brenguier et al., 2007; Jousset et al., 2010a). However, seismic data alone cannot give a complete picture of the reservoir.

Resistivity methods are widely used to investigate crustal structures in geothermal areas (e.g. Ussher et al., 2000) and complement seismic methods. Árnason et al. (2010), Kristinsdóttir et al. (2010) and Milsh et al. (2010) have shown that, at temperature below 350°C, resistivity (and P-wave velocity) in Icelandic fields have dependencies comparable to the rest of the world's geothermal fields (e.g. Newman et al., 2008). Low resistivity correlates with low permeability smectite alteration at temperature below 200°C. High resistivity prevails from 200°C to a much greater depth where, in some areas in Iceland, low resistivity has been attributed to a variety of potential causes unconfirmed by rock physics measurements, including magma melt and hyper-saline fluid trapped at the brittle/ductile transition. One objective of passive seismic survey is to constrain the ambiguity in the interpretation of deep features based on resistivity patterns alone.

Structural features of geothermal systems and their relationship with seismicity requires independent estimates of seismic velocities and resistivity that may be jointly interpreted. In this paper, we present structural features of the geothermal system at the Hengill volcano inferred from the comparison between a resistivity model obtained from 3D inversion of magnetotelluric (MT) and transient electromagnetic (TEM) data (Árnason et al., 2010) and a tomographic seismic model described in this work.

The Hengill volcano in Iceland is located about 30 km northeast of Reykjavik and has a high-temperature geothermal system (Bödvarsson, 1961), which has been exploited to produce fluid and heat for many years. The structure of the Hengill volcano has been studied by a number of authors using geological mapping and seismological 3D tomography techniques (Foulger, 1988a; Foulger and Toomey, 1989; Foulger et al., 1995; Saemundsson, 1995; Evans et al., 1996; Julian et al., 1997; Miller et al., 1998; Tryggvason et al., 2002), together with analyses of earthquake source mechanisms (Foulger and Long, 1984; Foulger, 1988b; Foulger et al., 1989; Miller et al., 1998) and of earthquake swarms (Sens-Schönfelder et al., 2006). These studies have helped to reach a high success rate for exploration drilling; 90% of exploration wells are productive when drilled in the area. However, owing to the high cost of exploration wells (about 4 million USD each), a better accuracy in the position of the productive faults would help in reducing the risk of drilling low productivity wells. Because of its particular geodynamical context, the Hengill geothermal system structure is one of the most studied in the world; therefore, it is a natural laboratory to test new exploration and monitoring techniques, like broadband seismology, aimed at improving our knowledge of structural and dynamic behaviour of geothermal systems. Some questions remain unanswered, such as the possible existence of a partial melt body and/or supercritical fluid at depth (Tryggvason et al., 2002). At present, geothermal fluids are produced from a depth of about 2 km, but the ongoing Iceland Deep Drilling Project (IDDP) aims at extracting supercritical fluids from a depth of about 3 to 5 km (Fridleifsson and Elders, 2005).

To derive an integrated model of the Hengill geothermal system, we carried out geophysical observations in the framework of the IGET (Integrated Geophysical Exploration Technologies) European Framework Program 6 project (Cumming and Bruhn, 2010). The inversion of a series of TEM soundings and MT profiles provided the resistivity model (Árnason et al., 2010), and a local earthquake tomography survey provided velocity models. Setting up a temporary seismological network with seven broadband seismic stations in the Hengill volcanic area supported two different objectives:

1. These seismic data support earthquake location and V_P and V_S tomography analyses that, together with the complementary 3D MT resistivity imaging, will constrain the geological structure to depths of 0-5 km beneath Hengill volcano. The study includes both natural seismicity associated with the triple junction and induced seismicity associated with the exploitation of the geothermal system. This builds on previous tomography studies carried out at Hengill volcano (e.g., Toomey and Foulger, 1989) that revealed the main structural features of the volcanic area and the triple junction. In particular, the V_P/V_S ratio and attenuation measurements are diagnostic of pore-fluid and temperature conditions when used in conjunction with V_P (Evans et al., 1994; Gunasekera et al., 2003; Husen et al., 2004).

2. In a separate study (Jousset et al., 2010b), the broad-band seismic data support analysis of the frequency content of the (micro)earthquakes, particularly long-period (LP) events that may be related to non-double couple events previously identified at the Hengill volcano in the 1980s. These events are thought to be possible signatures of fluid movement linked to the geothermal exploitation (Miller et al., 1998). Broadband seismometers allow the acquisition of broadband signals, like long-period (LP) earthquakes (0.5 s to 5 s), tremors, and very-long-period (VLP) earthquakes (above 5 s) (e.g., Jolly et al., 2010), having specific characteristics described mainly in terms of duration and frequency content, that are related to resonances of fluid-filled cavities like cracks (Chouet, 1996) or conduits (e.g., Jousset et al., 2003; 2004).

In the present paper, we focus on the first objective above, improving the resolution of structural features within the Hengill geothermal field, by deriving a seismic velocity model from tomography based on the local seismicity acquired for this project and integrating the resulting velocity model with the resistivity model of Árnason et al. (2010) into a common interpretation. The second objective is the subject of another work (Jousset et al., 2010b) which uses results of this study. After giving a brief description of the Hengill geological setting in Section 2, we describe the seismological data acquisition and processing in Section 3. The strategy for performing the tomography inversions is outlined in Section 4. In Section 5, we describe our method to integrate the results of the velocity model and the resistivity model. Finally, conclusions appear in Section 6.

2 The geothermal field at Hengill volcano within the triple junction tectonic setting

2.1 Geological setting of the Hengill Volcano Complex

The Hengill volcanoes are located at the intersection of three tectonic systems (Ingolfsson et al., 2008):

(1) the Reykjanes Peninsula, which is the topographic expression of the Reykjanes Ridge spreading between the North American and European plates to the south

(2) the West Volcanic Zone, which expresses the spreading between the North American and European plates to the north

(3) the South Island Seismic Zone, which is a transform zone from the West to the East Volcanic Zone

Therefore, the area is a triple junction, favorable to the rising of magma pulses and associated heat (Foulger, 1995). An intense fissure swarm crosses Hengill volcano (Figure 1) and extends from the coast to the south of Hengill volcano and to the north of Lake Thingvallavatn. At the eastern edge of Hengill volcano lies a second volcano called Hrómundartindur, and a third volcano Grensdalur is located to the south.

2.2 The geothermal system at Hengill Volcano Complex

The Hengill volcanoes were found in the late 1960s to have high potential for geothermal energy production (Gunnarsson et al., 1992). The natural geothermal activity is expressed by numerous hot springs and fumaroles spread throughout the area around the three central volcanoes (Figure 1), (Saemundsson, 1995; Arnórsson et al., 2008). The heat loss is about 350 MW. Steam and hot water for electricity generation and space heating are located near the volcanic centres at the Hengill geothermal system (Figure 1), within a fissure zone and a graben characterised by both porous matrix and anisotropic fissure permeability (Bjornsson et al., 2003; Gunnarsson et al., 2010). Two fields are at present exploited: Nesjavellir, in the northern sector and Hellisheidi in the southern sector. The Bitra and Hverahlíd fields are being explored to the east and south of Hengill central volcano, respectively (Franzson et al., 2010). The Nesjavellir Field (Figure 1) supports the first power plant installed in the Hengill area. Based on extensive exploration studies (Gunnarsson et al., 1992), over 20 wells up to 2.5 km in depth have been drilled. Reyjavik Energy operates a 90 MWe power plant and produces 200 MWt of thermal energy for space heating in the Reykjavik area, 27 km away. Production at the Hellisheidi Field to support 210 MWe generation began in 2006 (Gunnarsson et al., 2010). Injection wells for the fields in the Hengill area (Hardarson et al., 2010) are located south of the production areas.

2.3 Tectonic, volcanic activity and seismicity at Hengill volcano

Recent tectonic and magmatic activity has been associated with the Hengill volcanic system since the center of volcanic production shifted westward from Grensdalur to the Hengill system 0.5 Ma ago (Ingolfsson et al., 2008), although Grensdalur has probably been active more recently than 0.5 Ma (Kristjan Saemundsson, pers. comm., 2008). Apart from a small eruption in 1789 at Hengill volcano, which accompanied the last rifting episode, the last major eruption occurred about 2000 years ago. Between 1952 and 1955, several earthquake swarms occurred in the Hengill area and ended with a magnitude 5.5 event in 1955. In 1994 intense swarm activity started at the Hengill area beneath Hrómundartindur volcano, with several thousand events above magnitude 0.5 recorded by the South Iceland Lowland (SIL) network (Stefánsson et al., 1993; Jakobsdóttir, 2008). In March 1995, the activity spread to the Ölfus area, about 10 km south of the Hengill and Hrómundartindur volcanoes. This activity stopped in mid 1996; a second sequence that started in 1997 culminated with two magnitude 5.5 earthquakes in June and November 1998. Over 90,000 earthquakes were located altogether in this episode. In mid-1999 the activity returned to the pre-1994 level. Repeated geodetic measurements and InSAR detected uplift (7.5 centimeters) centered south of Hrómundartindur volcano and expansion between 1986 and 1995 in the southeastern area of the Hengill volcano (Sigmundsson et al., 1997; Feigl et al., 2000). This activity is interpreted as a small magma intrusion of about 1 to 3×10^7 m^3 and modelled by a Mogi (1958) source at a depth of about 7 km (Feigl et al., 2000). Pedersen et al. (2007) attributed the production of so many earthquakes by such a small intrusion to the low background stress level.

The intense seismicity at Hengill volcano and in southern Iceland has been the subject of several local earthquake tomography studies. In 1981 a temporary network of 23 analogue seismic stations with vertical component seismometers recorded 2000 locatable earthquakes (Foulger, 1988a; 1995), from which a 3D distribution of compressional-wave speed V_P was obtained (Toomey and Foulger, 1989; Foulger and Toomey, 1989) with a resolution of 2 km horizontally and 1 km vertically. In 1991 a temporary network of 30 seismic stations with short-period three-component sensors continuously recorded ground motion with a sampling rate of 100 Hz for two months. From about 4000 recorded earthquakes, inversion of 228 well-distributed earthquakes and one explosion supported the tomographic imaging of seismic velocity in a volume about three times larger than the volume analysed in 1981 (Foulger, 1995; Miller et al., 1998), but the resolution was not improved. Tryggvason et al. (2002) analysed nine years of the SIL records (Jakobsdóttir, 2008) comprising about 75,000 earthquakes to perform a more regional tomography of southwest Iceland, with a special focus on the Hengill Triple Junction. The resolution of the model is 4×4 km due to the great distance between seismic stations of the SIL network.

These seismic studies reveal the main structures of the volcanic area and the triple junction at Hengill, but their resolution is not sufficient to infer details of the geothermal field suitable for drilling. In the present study, we perform 3D tomography (Section 4) on earthquake records from a four-month long survey using high-quality, continuous broadband recording described in Section 3, and we integrate our results with a resistivity model (Section 5).

3 Data acquisition and processing

Our network included two CMG-40TD (0.016-50 Hz) Güralp and five CMG-ESP (0.008-50 Hz) Güralp broadband three-component seismometers (Figure 1). The stations recorded ground motions continuously with a sampling rate of 100 Hz from June to October 2006. Digitized data were stored on local hard disks. A detailed description of the broadband network, station set-up and data processing can be found in Jousset and Francois (2006). In addition, we used three stations from the permanent SIL network (Stefánsson et al., 1993; Jakobsdóttir, 2008), set to continuously record data during the four months of our study. Compared to previous tomographic studies (e.g., Foulger and Toomey, 1989), we designed our network to image the known locations and focal depths of earthquakes (depths of about 1-5 km) (e.g., Jakobsdóttir, 2008). Therefore, the network coverage is smaller than the coverage of Foulger and Toomey (1989) networks, but the station density is about the same and even denser around Olkelduhals, as shown in Figure 1.

3.1 Earthquake detection, classification and catalogues

To detect events, we performed a Hilbert transform on each of the three components of the continuous data and computed the ratio between the STA (Short Term Average, using 0.5 s of data) and LTA (Long Term Average, using 10 s of data) of the velocity amplitude at each station. An event is detected when the STA/LTA ratio exceeds a threshold (fixed at 2 for our data set), for the three components at the same time. When an event is detected at four (or more) stations of our network, the waveform of the signal (one minute of data, with 15 seconds before the trigger and 45 seconds after the trigger) is extracted for all stations from the continuous data and classified according to the number of stations that detected the event. Once event detection and automatic classification have been performed, a further analysis of each waveform at each station is performed to extract as much information as possible from the data. We used an interactive integrated program written in Matlab for analysis of data from local seismic arrays (Jousset, 2006).

This approach allowed us to detect and classify more than 600 events from June 2006 to October 2006. These events included 500 volcano-tectonic microearthquakes located within the Hengill area, 40 tectonic earthquakes originating from outside the Hengill area, and 30 long period events, among which 10 are thought to be within the Hengill area (Jousset et al., 2010b). Note that the SIL network recorded 130 locatable earthquakes for the same period of time, all of which were detected by our algorithm. The rate of seismicity is more than four events a day with some periods of several earthquakes per minute. The analysis of all event types is described in Jousset et al. (2010b).

3.2 P- and S- arrival times picking method

The joint inversion for hypocentre location and 3D velocity model tomography was performed using volcano-tectonic earthquakes, with clear arrival times for P- and S- waves on at least four stations. Computer assisted visual picking was employed to accurately pick the compressional (P) and shear (S) arrival times required for the tomography. To ensure better control on the quality of the data set and also to apply the method to the picking of S-waves, which are more difficult to accurately pick using an automatic method, we did not use an automatic phase-picker (Allen, 1982; Zhang et al., 2003). To assist the visual picks, we implemented an algorithm that computes and displays picking criteria (Akaike, 1978) directly on the amplitude trace of the seismogram (Maeda, 1985), without using autoregressive coefficients as in methods like that of Leonard and Kennett (1999). For a digital seismogram $x[1,N]$ of length N samples, the Akaike Information Criteria (AIC) value is defined as:

$$\mathrm{AIC}(k) = k \log\left[\mathrm{var}(x[1,k])\right] + (N-k-1)\log\left[\mathrm{var}(x[k+1,N]\right] \qquad (1)$$

in which k ranges through all the seismogram samples, *var* means the variance, and log is the natural logarithm. When selecting windows where a wavelet is located, this AIC picker defines the onset point as the global minimum (Figure 2). This picking method minimizes operator errors. Our broadband data also includes oceanic microseisms, which affect the AIC values, preventing accurate picking unless filtering is applied. The best picking results were obtained when data were filtered in the range 1 to 30 Hz. We extracted 339 earthquakes with clear P- and S- arrival times detected by at least 4 stations (2266 P- and 2432 S- arrival times).

We also implemented an estimate of picking uncertainty. The uncertainty is estimated by the use of two picking values instead of only one, as is usually done. The two picked times define a time interval during which the wave arrival time might be located, assuming uniform probability. Figure 3 shows the statistics on the time interval for P and S picks, quantifying the uncertainty of our data set. These statistics are used to define the pick quality required by the tomographic inversion algorithm (Kissling et al., 1994). The time interval that includes 95% of the pick uncertainty values is divided into four sub-intervals, each allocated to a pick quality. For instance, an interval of 0.06 s includes 95% of the pick uncertainty values for P-picks (Figure 2). Pick quality numbers indicating decreasing quality from 1 to 4 are allocated to time intervals (0-0.015 s, 0.015-0.03 s, 0.03-0.045 s, 0.045-infinity).

3.3 V_P/V_S ratio from Wadati diagram analysis

A global first estimation of the mean V_P/V_S ratio can be determined by using the Wadati diagram in which the S-P differential time is plotted against the P-arrival time (Wadati, 1933) or the S-arrival time is plotted against the P-arrival time (Chaterjee et al., 1985). The V_P/V_S ratio is then calculated from the slope, which provides a starting model for tomographic inversions.

The Wadati diagram analysis can also be used to detect and remove outliers in the picked arrival times for each earthquake. These will cause V_P and V_S points to plot far outside the corridor defining the V_P/V_S ratio. These bad points indicate bad P or bad S picks, or both: we either removed them from the data set, or we inspected the seismograms to check picks. From the 341 earthquakes in our data set, errors mainly result from bad S– wave picks for the more remote stations, HEI and SAN. S– to P– wave conversions at structural features might have led to confusion between phases. Errors in the P– pick may have occurred because of low signal/noise ratio. We removed 17 earthquakes and corrected picks for about 25 earthquakes.

After bad picks had been corrected, we applied the Wadati diagram analysis again to the reduced data set (322 earthquakes). We also computed the histogram of the P and S pick couples per event used for the Wadati diagram. We found 3, 39, 43, 67, 52, 56, 43 and 36 events that had a number of picks 3, 4, 5, 6, 7, 8, 9 and 10, respectively. The median number of P and S pick couples per event is 7. A V_P/V_S ratio of 1.75 +/-0.12 provides the global fit to all pairs of earthquake picks (Figure 4). We also computed the V_P/V_S ratio for each earthquake separately, and averaged these ratios to find that V_P/V_S =1.765 +/-0.15. These values reflect a typical range of V_P/V_S ratio for crustal rocks, similar to those inferred from previous data analysis in the Hengill area: Foulger (1995) and Miller et al. (1998) found V_P/V_S =1.77 and Tryggvason et al. (2002) obtained V_P/V_S =1.78.

4 Joint hypocentre location and 3D tomography

The theory and method of local tomography inversion have been described by a number of authors (e.g., Thurber, 1983; 1986; 1993; Kissling, 1988; Ellsworth et al., 1991; Eberhart-Phillips, 1993; Iyer and Hirahara, 1993; Kissling et al., 1994; Eberhart-Phillips and Michael, 1998; Tryggvason et al., 2002; Koulakov et al., 2007).

4.1 *A priori* hypocentre location for inversion

Many tomographic studies (Thurber, 1983; Eberhart-Phillips, 1990; 1993; Eberhart-Phillips and Michael, 1998), invert local earthquake arrival times for hypocentre locations and velocity structure in two steps: 1. joint inversion for the 1D velocity model and hypocentre locations, followed by 2. joint inversion for the 3D velocity model and hypocentre locations.

To test the effect of variations in the *a priori* hypocentre locations on the results of the velocity inversion, we invert our data set using velocity models of increasing complexity. We perform preliminary independent hypocentre location inversions using either a homogeneous P-wave velocity model of 5 km/s for inverting P-picks only or a homogeneous S-wave velocity model of 2.8 km/s for inverting S-picks only; the P- and S-wave velocities are taken from previous studies at Hengill (Foulger, 1995; Miller et al., 1998; Tryggvason et al., 2002). To estimate hypocentre locations, we implemented a grid-search nonlinear inversion procedure in which travel times are computed at each station for sources located at regularly spaced nodes (300 meters) of a 3D grid sampling the volume beneath Hengill volcano (17 km E-W × 20 km N-S × 10 km deep). Grid searches to independently fit P-picks and S-picks reveal that most earthquake hypocentre locations fall in the central area of our network. Using these *a priori* hypocentre locations, we then performed the two-step tomography approach applying a 1D model inversion code VELEST (Kissling et al., 1994) and a 3D model inversion code SIMULSP12 (Thurber, 1993; Evans et al., 1994). The 1D code VELEST (Kissling et al., 1994) provides 1D V_P (and V_S) models as a starting point for the 3D inversion (Eberhart-Phillips, 1993). The velocity structure of the geothermal reservoir is imaged by applying tomographic inversion to the local earthquakes with the computer program SIMULSP12 (Thurber, 1983; Evans et al., 1994; Thurber, 1993; Eberhart-Phillips, 1993) that solves simultaneously for earthquake locations and crustal structure by an iterative damped-least-squares method.

4.2 VELEST 1D inversions

The first step involves running VELEST on the station location and arrival time data for the 322 detected earthquakes and jointly inverting the earthquake hypocentres, the 1D velocity model used in the hypocentre computation, and the station corrections used to adjust residual errors that are likely due to near-surface effects. An initial test indicated that the use of only P-wave arrival times leads to improbable results (P-wave velocities are not realistic). We invert the V_P model first, using both P-wave and S-wave arrival times and assuming a constant V_P/V_S ratio.

Following Husen et al. (1999), for each set of the performed inversions we used a wide range of starting velocity models to estimate the resolution of the 1D inverted model, assuming a constant V_P/V_S ratio of 1.76. We invoke two *a priori* hypocentre assumptions: the location and depth previously computed from the grid search or the location of the centre of the network (station HE3) and a depth of 4000 m. Both *a priori* hypocentre assumptions produce similar results for the velocity model and hypocentre locations. For all inversions, the station correction is inverted by fixing the correction at station HE3 to be zero. Station corrections are positive for the stations (HEI, KRO and SAN) located outside Hengill volcano, whereas station corrections within the network (HE1 to HE7) are all negative.

Figure 5 shows the final result of the 1D inversion with P- and S- arrival times. The small aperture and the small number of earthquake are probable reasons for the lack of conformity with previous models at depths of 5 to 7 km. Data variance from the inversion for the 1D model is RMS=0.08192. This P-wave velocity model is used as the initial model for inverting the V_P/V_S ratio. We use the same approach to invert for the 1D model of the V_P/V_S ratio.

4.3 3D inversion using SIMULPS12

The second step of the tomography involves inversion of the P- wave velocity model using the V_P 1D model (Figure 5) and V_P/V_S =1.76 as *a priori* information in the program SIMULSP12 (Evans et al., 1994). We vary the V_P/V_S values as starting models in subsequent inversions. Following Evans et al. (1994), we first filtered out all earthquakes for which the azimuthal distribution of stations around the epicenter left an angular gap greater than 180°. The number of earthquakes in the reduced data set dropped to 249 earthquakes.

Several methods can be used to parametrize the structure (see appendix). To parametrize the structure, we assigned values of V_P and V_P/V_S ratio to the nodes of a 3D grid. The observed P- and S- arrival times are inverted to simultaneously determine the coordinates of earthquake hypocentres and the values of V_P and V_P/V_S at the grid nodes. Trilinear interpolation is used to estimate V_P and the V_P/V_S ratio between the nodes. Ray paths are calculated with an approximate 3D ray tracing algorithm that produces curved, nonplanar ray paths defined by points more finely spaced than the velocity grid. The solution is obtained by iterative damped least-squares inversion (Evans et al., 1994). For each iteration, new ray paths are determined and the hypocentre solution is computed. Weighting is applied to each observation based on the size of the travel time residual and source-receiver distance.

A damping parameter is used to stabilize the inversion (Eberhart-Phillips, 1986). Prior to each 3D inversion, the damping parameter is chosen empirically by evaluating the trade-off between data and model variances in one-step inversions (Eberhart-Phillips, 1986). The data variance is computed from observed and computed travel times and the model variance is computed from the 3D velocity variation with respect to the 1D model. The optimal value of the damping is the one for which the data variance is minimum with a reasonable model variance.

4.4 Resolution and robustness of models

The distributions of the sources and stations yield a model volume that is irregularly sampled by seismic ray paths. Estimating model fidelity or resolution in earthquake tomography may be performed by several means, such as inspecting the diagonal elements of the resolution matrix (Roeker, 1982), or by evaluating reconstructed synthetic models (e.g., checkerboards) for specific earthquake or station geometry (Humphreys and Clayton, 1988; Eberhart-Phillips and Michael, 1998).

The model resolution matrix describes the distribution of information for each node, such that each row describes the resolution of a model parameter and how well the information has peaked at this particular node or smeared to adjacent nodes (Thurber, 1993; Eberhart-Phillips and Reyners, 1997; Eberhart-Phillips and Michael, 1998; Yao et al., 1999). It provides information necessary for interpreting the distribution of ray-paths (Figure 6) and the degree and pattern of smoothing. Michelini (1993) computes the resolving width, S_j, for a grid point from all the elements, s_{ij}, of the corresponding row of the resolution matrix, weighted by their distance, D_{jk}, from the grid point,

$$S_j = \log\left[\left| s_j \right|^{-1} \sum_{k=1}^{N} \left(\frac{s_{kj}}{\left| s_j \right|} \right) 2D_{jk} \right] \qquad (2)$$

This measure also takes into account how much smearing into adjacent nodes is present. A similar measure is given by the spread-function SF_j of node j as defined by Toomey and Foulger (1989). It is calculated from the sum of all elements of the corresponding row of the model resolution matrix r_{kj} weighted by their distances D_{jk} to the particular node:

$$SF_j = \log\left[\left| r_j \right|^{-1} \sum_{k=1}^{N} \left(\frac{r_{kj}}{\left| r_j \right|} \right) D_{jk} \right] \tag{3}$$

The size of the model resolution matrix often makes complete examination not feasible. On the other hand, the restriction to only the analysis of the diagonal elements is not sufficient because it neglects the valuable information contained in the off-diagonal elements. Furthermore, the size of the diagonal elements is strongly dependent on the damping and the dimension of the grid used in the inversion.

The spread function therefore considers both the amount of information and its smearing. Large diagonal elements result in small *SF*-values, whereas significant values of off-diagonal elements, especially of distant nodes, result in larger *SF*-values. Figures 7 and 8 show these spreads for example sections. These figures show where the tomography is well resolved, by clipping out zones where the resolution given by the resolution matrix is too low and using a grey color scale to quantify the resolution.

Using a checkerboard test, we further evaluate the scale of seismic velocity variations that could be resolved by tomographic inversion of data collected using our acquisition geometry. The synthetic velocity model includes a 3D checkerboard pattern of positive and negative 5% perturbations in seismic velocity relative to the 1D velocity model. Synthetic travel times are computed in the perturbed model for the real hypocentre and station distribution. We invert the synthetic travels times (to which a normal error distribution with rms=0.02 s is added) by starting from the 1D velocity model. The reconstruction of the checkerboard is successful where the tomographic cells (velocity parameters) are sampled by enough rays (Figure 6). Results of the checkerboard tests performed with a grid node spacing of 1 km and an anomaly size of 2 km show that the reconstruction is good in the center of our network (see Figures 9, 10 and 11). Away from the network, the image is not resolved, as cells are crossed by a small number of rays (Figure 6).

For the inversion of the real data, we started with a coarse 3D grid with a spacing of 2 km, with several nodes outside the target geothermal system, to constrain the volume that our dataset could image. In a second step we refined the grid by using a grid node spacing of 1 km to model the subsurface. After we inverted for the V_P/V_S ratio with grid spacing 1 km, the final RMS error is 0.041 s. Inversions performed with different grid spacings produce similar features (Figures 12 and 13), which implies that observed features are robust. The area of resolution is slightly reduced with 1-km grid spacing, especially at the edges of the network. Still, the grid spacing of 1 km produces excellent image fidelity without serious loss of resolution for the critical region directly below our network.

We conclude that velocity variations with a scale of about 2 km or larger can be identified using a 1-km resolving grid within the perimeter of the seismic network and at depths shallower than 5 km, a range that encompasses the targeted geothermal reservoir.

4.5 Results

Final results for the P- wave velocity are shown in horizontal slices at different depths (Figure 12) and in NS and EW cross-sections (Figures 13 and 14). The same iterative approach has been used to invert for the V_P/V_S ratio and earthquake hypocentres (Figures 15 and 16).

Distribution of earthquakes

Local seismic events (predominantly volcano-tectonic events) are found at depths between 1 and 6 km beneath our network. Several individual clusters (at least 4) can be identified, all within the aperture of the network. A first cluster (21.3 W, 64.09 N) of about 15-20 earthquakes is located within Hengill volcano to the south of Nesjavellir at a depth of 2 to 3 km (Figures 12 and 14). These earthquakes might correspond to stress changes related to geothermal production at Nesjavellir. The second cluster (21.23 W, 64.05 N), the third cluster (21.24 W, 64.07 N), and the fourth cluster (21.26 W, 64.06 N) lie around HE3 station, between 2 and 5 km depth, within a rock volume with low P-wave velocity and high V_P/V_S ratio. Most of the seismicity is located above a deep electrical conductor (Árnason et al., 2010). In addition, their location is consistent with the heat source at depth near Bitra described in the conceptual model of Gunnarsson et al. (2010).

We interpret these earthquakes as resulting from stress changes within the geothermal reservoir where hot fluid rises in the crust above the heat source. Note that the locations are at the intersection of faults inferred from the long-term seismicity (Árnason et al., 2010), as shown in Figure 17 on the resistivity maps. A possible explanation for stress change could be heat exchange from depth between different parts of the geothermal system, as proposed by Geoffroy and Dorbath (2008). We further discuss this hypothesis in the light of the tomography results. Tryggvason et al. (2002) report clusters of deep earthquakes occurring at about 10 km depth, below the brittle/ductile transition at 5-6 km depth, which they attribute to a change in the strain rate of the spreading rift. We did not observe such deep earthquakes during our experiment.

Cooling, mostly through natural heat loss and consequential thermal contraction and cracking in the heat source has been proposed as the cause of the continuous small-magnitude earthquake activity in this area (Foulger and Long, 1984). This mode of earthquake induction was suggested following the observation that many of the earthquakes have non-double-couple focal mechanisms with large explosive components. The mechanism responsible for those non-double-couples may be fluid flow into newly formed cracks (Miller et al., 1998; Sens-Schönfelder et al., 2006). Jousset et al. (2010b) discuss the source mechanism of the observed long-period (LP) earthquakes and relate them to fluid exploitation, rather than to magmatic activity. Such LP earthquakes may be related to the resonance of part of the hydrothermal system, such as fractures filled with gas or supercritical fluids and could be triggered by pressure changes with sudden variations in the fluid flow rate at start-up or shut-in of geothermal production and injection.

V_P structure

Our results reveal a high V_P body southeast of the Olkelduhals area at depths ranging from 0.5 to 4 km (area A in lower left map in Figure 12). V_P varies laterally by about -10% to +10% from its average value within each layer. This observation is also reported by Foulger and Toomey (1989) and Miller et al. (1998). We also find low velocity bodies at 1 km depth in two areas, 1) north-west of Olkelduhals, south of Mount Hengill and 2) below Nesjavellir exploitation wells, indicated as areas B1 and B2 in lower left map in Figure 12 and upper left map in Figure 17. These low velocity bodies are collocated with high temperature anomalies measured in wells (Gunnarsson et al., 2010).

At about 4 km depth, Foulger (1995) found a small (about 5 km^3) low-V_P velocity anomaly (about -7 %) beneath the northern edge of Mount Hengill that she interpreted as a small volume of partial melt. This body was not confirmed later by the tomography of Foulger et al. (1995). At this location (below Nesjavellir), our tomography reveal a possible high-V_P velocity body, but its exact extension is not well resolved because our experiment lacked deep seismicity.

V_P/V_S structure

The V_P/V_S ratio varies by 6% throughout the maps at six depths from 1 to 4 km shown in Figure 15. The most coherent anomaly is an elongated low-V_P/V_S feature at 0 to 2.5 km depth that is aligned with the trend of the hot springs along its eastern margin. This body strikes N-NW, whereas the fissure swarm strikes NE in the Hengill area (Figure 1). At 3-4 km depth, low V_P/V_S values extend beneath the northern part of Hengill volcano, to the south of Olkelduhals area and to the east, although the checkerboard test in Figure 16 shows that its full extent is not well resolved. These bodies may be the low-V_P/V_S ratio area found by Tryggvason et al. (2002), with a better resolution.

For solid rock, seismic velocities and the V_P/V_S ratio can be defined using the effective bulk and shear moduli, which are dependent on rock matrix moduli, pore fluid content, pore pressure, porosity and temperature. For fluid-saturated rocks, effective bulk and shear moduli can be computed by Gassmann's equations (Gassmann, 1951). The Gassmann equations are valid at seismic frequencies for a statistically isotropic pore space for any pore geometry. V_S is sensitive to rock matrix properties, especially rigidity related to induration and high rank alteration. It is less sensitive to porosity, except as it relates to rigidity and density. V_S is much less sensitive to the free gas to water ratio. V_P is more sensitive to porosity. If free gas is less than a few percent by volume, a small increase in gas will cause a large decrease in V_P due to the much higher compressibilty of gas. After gas exceeds a few percent, further increase causes V_P to increase slowly.

Husen et al. (2004) computed theoretical changes of V_P/V_S and showed that a change in pore fluid from liquid to gas produces a significant decrease in V_P/V_S at high porosity. At Hengill, the porosity is less than 15% (Miller et al., 1998). According to Husen et al. (2004), a porosity of 10% causes a decrease of 8% in V_P/V_S ratio, which is a bit larger than what we observe in our tomographic images. Associated with the low V_P/V_S ratio at shallow depths, we observe a high V_P anomaly in the southwest part of the area, excluding gas as the cause of the low V_P/V_S ratio, and a low V_P anomaly in the northwest, where gas could be the cause of the low V_P/V_S ratio. As shown in Figure 15, many hydrothermal features are located along the elongated V_P/V_S anomaly, suggesting the existence of hot conduits, where fluids circulate up to the surface.

According to Árnason et al. (2010), much of this trend is correlated with a low-rigidity, low–permeability, relatively shallow clay cap, and thermal manifestations occur at gaps in this cap where structures or unaltered formations connect the thermal manifestations through the base of the clay cap to the immediately underlying reservoir, generally less than 2000 m deep and sometimes less than 500 m deep. Moreover, Gunnarsson et al. (2010) and Bjornsson et al. (2003) suggest that many of the springs and fumaroles along this trend mark outflows, not only upflows.

Small melt pockets were suggested by previous studies (e.g. Foulger, 1995; Feigl et al., 2000). It is possible that a magma body could be associated with the high V_P/V_S values which form an elongated anomaly extending below 2.5 km in the central part of the study area. However, the cut-off depth of the seismicity is much deeper (about 5 to 6 km); according to temperature gradients observed in wells, a temperature of about 665°C (Tryggvason et al., 2002) may be inferred at this depth. This temperature is too low for large magmatic bodies, but Árnason et al. (2010) suggested that dykes and magma intrusions might exist based on new resistivity results.

To either side of this central body, our results reveal separate low-V_P/V_S features. Tryggvason et al. (2002) attributed low *Vp/Vs* ratio to the existence of supercritical fluids. We discuss this issue in the next section by integrating our velocity models and the resistivity model (Árnason et al., 2010).

5 Integrating velocity and resistivity structures

The integration of observations from different geophysical techniques is a way to increase our knowledge of the structure of geothermal systems. Several geophysical techniques have been applied to study the structure of the Hengill high-temperature area (Bjornsson et al., 1986; Gunnarsson et al., 1992). Within the IGET project, transient electromagnetism (TEM) surveys and 3D magneto-telluric (MT) profiles have been acquired over the area (Árnason et al., 2010). Figures 17, 18, and 19 compare the tomography results with the 3D resistivity inversion results of Árnason et al. (2010). At about 2 to 3.5 km, where most of the seismicity occurs, a change in seismic and electrical parameters also appears to occur. These changes may reflect changes in rock alteration or fluid physical properties.

5.1 High-temperature Hengill geothermal system resistivity structure

The resistivity structure of high-temperature geothermal systems in basaltic rocks has been summarized in Árnason et al. (2010), which also describes the acquisition and 1D and 3D inversion of new transient electromagnetic (TEM) and magnetotelluric (MT) observations in the Hengill area. Inversion of this TEM and MT data set reveals a low resistivity vertical cylindrical body below Olkelduhals at depths of 3 to 4 km, and an elongated low resistivity anomaly oriented NW-SE at greater depths. Árnason et al. (2010) discuss the nature of these conductors. First, they describe the structural relationships between geological data and the resistivity model above 2 km, where well data is available. Second, the low resistivity at 4 km depth corresponds to solidified dikes and magmatic intrusions, which provide the heat source for the geothermal system above. However, no indication is provided as to which property of the dikes or the intrusions makes them conductive.

5.2 Integration of velocity and resistivity models

Figure 17 shows a comparison of the results of the 3D resistivity model (Árnason et al., 2010) and our V_P velocity and V_P/V_S ratio models for the depths between 2.5 and 3.5 km where V_P, V_P/V_S and resistivity show significant changes.

There are two approaches to establishing relationships among rock properties: establishing relationships using rock physics models, and formulating empirical relationships directly between the properties of interest (Harris and MacGregor, 2006). The first approach is based on theoretical models that predict the variation of rock properties with respect to some underlying rock parameters, such as the Archie equation relating resistivity to porosity for clay-free rocks (Archie, 1942) and the Gassman equations relating seismic velocity to porosity for consolidated rocks (Ciz and Shapiro, 2007). In addition to rock physics models to relate resistivity or seismic velocity to parameters like porosity or temperature, this approach also requires empirical support for these relationships (e.g. Kristinsdóttir et al., 2010; Jaya et al., 2010). The second approach is to use suitable data to empirically fit a direct relationship between rock properties, such as between seismic velocity and electrical resistivity using the Faust equation for consolidated sandstones (Faust, 1953). A difficulty with both of these approaches is that the solution obtained may be biased if the relationship between the rock properties is not well described by the models or empirical equations.

An alternative way to investigate the relationships between resistivity and seismic velocities is by cross-plotting them (Munoz et al., 2010). In this work, we confirm the potential of this method to improve our knowledge of structural features at geothermal systems. We focus here on the link between the V_P/V_S ratio and resistivity to illustrate the great potential this method has for high-enthalpy geothermal systems.

We adapted to our case classification algorithms used to perform lithologic interpretations (e.g. Bauer et al., 2003). The seismic model (V_P/V_S ratio) and the resistivity model at the Hengill area were first considered as a set of grid cells representing the objects to be classified. As the velocity and resistivity inversions were performed independently, we first defined common grid cells, in which values of resistivity and V_P/V_S ratio are interpolated from their initial model into each cell of the common grid. Trilinear interpolation is used for both data sets. The choice of the interpolation is not critical for the final results. Each grid cell is therefore characterized by distinct values for the two attributes V_P/V_S ratio and resistivity. We used a grid cell of size 0.005 degrees (about 250 m).

To perform the classification, we plotted resistivity values for all cells as a function of V_P/V_S ratio values (Figure 18). Volumetrically large geologic units having homogeneous geophysical properties will plot as a single cluster, with many instances. Small geologic units, or those whose V_P/V_S ratios and/or resistivity values are highly variable and do not correlate, will be relegated to the background of the plot. We quantify the number of {resistivity, V_P/V_S ratio} couples that fall into a particular area of the cross-plot (defined as a class) using a 2D histogram technique. We did not use cluster analysis or probability density functions to identify classes. Instead, classes are taken as areas encompassing clear maxima in the 2D histogram. Limits of the classes defined by each maximum in the 2D histogram are given in Table 1. Slight differences in drawing class limits would change the limits of the specific zones in the geological medium, but it would not change main features. Figure 18 shows that we may define several classes of {resistivity, V_P/V_S ratio}, listed as classes 1 to 9 in Table 1.

To verify the hypothesis that each class in the distribution of {resistivity, V_P/V_S ratio} corresponds to specific zones in the geological medium, we plot the location of every couple belonging to one class on maps at several depths using a color scale. Figures 19 shows these maps at the three depths (see Figure 17) for classes shown in Figure 18 (see also Table 1). The geographic zones corresponding to classes defined in the 2D histogram are not random and correspond to geological features that can be differentiated by their combination of rock physics properties.

The most remarkable structure is the bean-shaped, class 8 and 9 feature at 3.5 km depth to the east of Hengill volcano. It trends southeast towards the seismically active area and the locations of hydrothermal manifestions. The overlying class 8 feature shown in the 2.9 km depth map indicates an onion-like layering of the parameter classes centered near the eastern edge of Hengill. Several classes above class 8 display the same onion-layer behaviour: going through the structure from shallow to deep, many of the classes are first located below the eastern edge of Hengill volcano and then spread around this central part, each defining a layer. For example, class 5 is located east of Hengill volcano at 2.3 km depth and spreads around this central area at 2.9 km depth, where it it appears farther north, to the east of Nesjavellir, and farther south, to the east of Olkelduhals. Below, the bean-shaped class body (classes 9 and 10) occurs at the center of the anomaly at 2.85 km depth and then spreads around to the sides at 3.5 km depth. The feature centered below the Hengill volcano may indicate the existence of a hot body having low resistivity and high V_P/V_S ratio, with a gradual variation of the parameters around it.

5.3 Discussion of the structure of the Hengill geothermal system

Based on results from previous investigations and this study, we have tentatively interpreted the classes of resistivity and V_P/V_S ratio shown in Figure 19 as a conceptual cross-section in Figure 20, showing the structural features of the hydrothermal system at Hengill volcano. Unfortunately, no cross-section or averaged corridor of sections was sufficiently populated by class data to illustrate the geometry more effectively than the sketch in Figure 20.

Recent observations from wells (Haraldsdottir et al., 2010) and surface geophysics (Árnason et al., 2010) have been used to infer the rock properties of the upper 2.5 km of the exploited geothermal fields at Hengill and have been integrated in a conceptual model of the Hengill geothermal system (Franzson et al., 2010). Like many other geothermal systems in the world, the Hengill geothermal system (Nesjavellir and Hellisheidi) comprises a low-resistivity layer underlain by higher resistivity. These structures are associated with alteration minerals having different electrical conductivity. In the low-resistivity cap, conductive alteration minerals in the smectite zeolite zone dominate (50-200°C). As temperature approaches 240°C, mixed-layer clays and then chlorite dominate with increased resistivity (Haraldsdottir et al., 2010). The temperature distribution given by the wells suggests that fluid movements are twofold: an up-flow above hot zones, where low resistivity and low-V_P/V_S velocity bodies are located (0-2.5 km depths) (e.g., Hengill volcano) and down-flow of cold fluids at the southern and western sides of Hengill volcano and Nesjavellir.

The interpretation of the deeper, elongated, low resistivity/high V_P/V_S ratio body (Figure 17) is more speculative. This body is located at the intersection of the faults inferred from long-term seismicity in the Hengill area (Árnason et al., 2010). It is also below a low-V_P/V_S ratio zone and the main trend of surface hydrothermal manifestations. Based on its low resistivity, Árnason et al. (2010) interpreted this feature as hot dikes or intrusions. This interpretation seems to suggest that a very small amount of partial melt might account for the low resistivity. The presence of supercritical fluids (Tryggvason et al., 2002; Franzson et al., 2010) has also been suggested in the Hengill area, at 3-4-km depth. The existence or the non-existence of supercritical fluid in geothermal systems is of primary importance as its heat capacity is much higher than that of fluid at subcritical conditions (e.g., Palmer et al., 2004). Two models are proposed for low rock resistivity at supercritical temperature: 1. the presence of magma, and 2. Fournier's model (Fournier, 1999) of hypersaline brines trapped below the ductile transition. Unfortunately, below the ductile transition, very little direct information is available. The Iceland Deep Drilling Project aims at drilling in those areas where supercritical conditions are expected (Elders and Fridleifsson, 2010; Lebert and Asmundsson, 2009; Halladay et al., 2010). Physical properties of supercritical fluids are known from laboratory experiments (e.g., Pitzer, 1983; Frantz and Marshall, 1984; Palmer et al., 2004). The critical point of pure water occurs at 22.1 MPa and 374°C. Large changes in the physical properties of water occur near its critical point and the fluid changes from polar to non-polar behaviour, resulting in a decrease of the dielectric constant of water and a decrease in the density.

In most high-temperature hydrothermal systems, fluid pressures are hydrostatic. In Iceland, the fluid pressures are close to boiling, and therefore the critical point should be reached at about 3.5 km depth (Elders and Fridleifsson, 2010). However, in several cases, temperature conditions higher than expected at a given depth have been encountered. For example, at Krafla caldera, drilling operations in 2010 encountered a magma body with supercritical conditions at a depth of 2100 m (Elders and Fridleifsson, 2010). The temperature below 2.2 km in well NJ-11 at Nesjavellir was over 380°C.

Rock physics experiments (e.g., Kummerow, 2005) show that, at supercritical conditions, rock elastic properties are dependent (like in the subcritical case) on several factors including the textural characteristics (grain size, grain shape, nature of grain contacts), the quantity and distribution of fluid, conditions of fluid circulation (drained or undrained), and temperature. In an impermeable rock, the increase of porosity due to thermal expansion of moist grain contacts has the same effect on elastic wave velocities as the increase of temperature by a factor of five (Kummerow, 2005). The effect of small amounts of intergranular supercritical fluid on the elastic properties of rocks can outweigh that of temperature. Velocity contrasts of several percent can be induced by the presence of small amounts of fluids on mechanically weak grain boundaries.

The V_P/V_S ratio increases with the reduction of pore volume due to an increase in the confining pressure. A linear trend appears between the logarithm of the resistivity ρ and V_P/V_S ratio (Figure 18), for $\log(\rho)<2.5$ (classes 5, 7, 8 and 9), expressed as $\log(\rho)=-85.3\ V_P/V_S + 151$. This trend may be related to the effect of porosity on both the electrical conductivity and the seismic velocities. Assuming that the resistivity ρ and V_P/V_S ratio have the form $1/\rho=f(\phi)$ and $V_P/V_S=g(\phi)$ where ϕ is the porosity, the relation is given by $1/\sigma=f[g^{-1}(V_P/V_S)]$. The investigation of the validity of such relationships in Hengill remains to be shown, but in the light of our results, we suggest that this trend corresponds to temperature increases with depth to the point that it exceeds supercritical conditions and causes small intergrain porosity variations that significantly affect seismic velocity.

The pattern of microearthquake hypocentres is interpreted to be an indicator of the transition between brittle and plastic behaviour at Hengill. In the Larderello geothermal field, supercritical fluids were found at the K-Horizon (3-4 km depth), and due to the high temperature prevailing at that depth, rocks are close to a plastic state (Bertini et al., 2006). Brittle-plastic conditions are strongly dependent on both temperatures and strain rates. Following Geoffroy and Dorbath (2008), we propose that the seismicity observed at Hengill is related to the brittle/ductile transition.

Bjornsson et al. (2003) and Gunnarsson et al. (2010) also addressed the issue of the temperature reversal at Hellisheiði using a simulation model with heat sources at >3000 m depth. These heat sources are constrained by measurements in wells to depths of 2500 m at Hellisheiði, Nesjavellir, Bitra and Hverahlíð and at least five wells located away from these fields, some near features interpreted in our work. Direct well measurements indicate that many of the thermal features are related to shallow outflows underlain by low-permeability volcanics.

6 Conclusions

We used travel time tomography to obtain an improved 3D velocity model of the Hengill geothermal system. The seismic network installed in the Hengill region allowed the construction of a high-resolution tomographic model with grid size of 1 km X 1 km horizontally. This high resolution, however, is limited to the region beneath the network. Our results confirm previous observations by Foulger (1995); Foulger et al. (1995) and Tryggvason et al. (2002).

We integrated our velocity models with a resistivity model obtained from TEM and MT inversion (Árnason et al., 2010). By using a classification technique in which clusters of {resistivity, V_P/V_S ratio} couples were identified, we discovered a low resistivity/high V_P/V_S ratio area at 2.5-4 km depths similar to the earthquake hypocentres and possibly extending deeper. We interpret this body as the heat source of the Hengill volcanic complex, because it may contain supercritical fluids. The extent of this feature is not well defined because of the limited velocity resolution. Above this body, where most seismicity is observed, hot, superheated (possibly supercritical) fluids would upflow in structural features like fault intersections related to the Hengill triple junction.

Although LP earthquakes are expected to have a non-double couple mechanism (Chouet, 1996) and a relationship between non-double couple earthquakes previously observed at Hengill volcano and LP earthquakes observed in this study are suspected, such a relationship has not been established. Further broadband seismic research in areas like Hengill may establish a more general relationship between non-double-couple and LP earthquakes.

One of the great advantages of studying geothermal systems targeted for economic purposes is that, on the one hand, they are much less dangerous than active volcanic systems that have hazards associated with magmatic and hydrothermal eruptive activity, and on the other hand they exhibit some of the same kinds of structural features and processes. Therefore, the study of geothermal systems may of great help in understanding structural and hydrothermal features at active volcanic systems. Our results may be extrapolated to hydrothermal systems around active volcanoes where drilling may be hazardous.

Acknowledgments

We would like to thank Michael Weber and Hubert Fabriol for their support. Kristin Vogfjörd and Steinunn Jakobsdottir are acknowledged for their help to this project and for providing the SIL data to this study. E.A. Gudnason, G. S. Hilmarsson, H. O. Stefánsson, J. E. Jónsson, S. A. Hálldorsson, Th. Agústsdottir and Th. Björnsdóttir provided valuable help during the (wet) field work. A special note of thanks to Benjamin Francois for his time and his nice music while driving on the beautiful icelandic roads to set up the seismic stations. Retrieving data from some disks would not have been possible without the help of Karl-Heinz Jäckel and Luong Van-Hung. Didier Bertil and Xavier Serey helped in analysing data. Fruitful discussions with Bryndís Brandsdóttir, Magnus Gudmundsson and Bernard Bourgeois are fully acknowledged. We acknowledge Gillian Foulger, Mitch Stark and two anonymous reviewers for their helpful comments that improved the manuscript. William Cumming provided insightful comments and suggestions on the final manuscript. John Douglas and William Cumming kindly improved the English. Many thanks to Sabodh Garg, the Associate Editor, for his patience and his involvement in the final editing. Five broadband instruments are from the GFZ instrument pool, and two from the BRGM instrument pool. This study was funded by the European Community in the Sixth Framework Programme though the IGET project (contract 518378) and ENGINE project (contract 019760).

References

Akaike, H., 1978. A Baysian analysis of the minimum AIC procedure. Annals of the Institute of Statistical Mathematics 30, 9-14.

Aki, K., Richards, P., 2002. Quantitative seismology. Second Edition. University Science Books, Sausalito, California, USA, 704 pp.

Allen, R. V., 1982. Automatic phase pickers: their present use and future prospects. Bull. Seismol. Soc. Am. 72(6), S225–S242.

Archie, G., 1942. The electrical resistivity log as an aid in determining some reservoir characteristics. Petroleum Technology 1, 55–67.

Árnason, K., Eysteinsson, H., Hersir, G., 2010. Joint 1D inversion of TEM and MT data and 3D inversion of MT data in the Hengill area, SW Iceland. Geothermics 39, 13-34.

Arnórsson, S., Axelsson, G., Saemundsson, K., 2008. Geothermal systems in Iceland. Jökull 58, 269–302.

Barnea, J., 1972. United Nations approach and accomplishments in the field of

geothermal resources development. Geothermics 1, 164–167.

Bauer, K., Schulze, A., Ryberg, T., Sobolev, S. V., Weber, M. H., 2003. Classification of lithology from seismic tomography: a case study from the Messum igneous complex, Namibia. J. Geophys. Res. 108 (B3), 2152-2167, doi:10.1029/2001JB001073.

Benz, H. M., Chouet, B. A., Dawson, P. B., Lahr, J. C., Page, R. A., Hole, J. A., 1996. Three-dimensional P and S wave velocity structure of Redoubt volcano, Alaska. J. Geophys. Res. 101 (B4), 8111–8128.

Bertini, G., Casini, M., Gianelli, G., Pandeli, E., 2006. Geological structure of a long-living geothermal system, Larderello, Italy. Terra Nova 18 (3), 163–169.

Bjornsson, A., Hersir, G., Bjornsson, G., 1986. Geophysical reconnaissance study of the Hengill high-temperature area, SW Iceland. Geotherm. Res. Council. Trans. 10, 205–210.

Bjornsson, G., Hjartarson, A., Bodvarson, G., Steingrimsson, B., 2003. Development of a 3D geothermal reservoir model for the greater Hengill volcano in SW-Iceland. In Proceedings: TOUGH Symposium 2003, Lawrence Berkeley National Laboratory, Berkeley, California, 1–11.

Bödvarsson, G., 1961. Physical characteristics of natural heat ressources in Iceland. Jökull 11, 29–38.

Brenguier, F., Shapiro, N. M., Campillo, M., Nercessian, A., Ferrazzini, V., 2007. 3D surface wave tomography of the Piton de la Fournaise volcano using seismic noise correlations. Geophys. Res. Lett. 34, L02305, doi:10.1029/2006GL028586.

Chaterjee, S., Pitt, A., Iyer, H., 1985. V_P/V_S ratios in the Yellowstone National Park Region, Wyoming. J. Volcanol. Geotherm. Res. 26, 213–230.

Chouet, B., 1996. New methods and future trends in seismological volcano monitoring. In: Monitoring and Mitigation of Volcano Hazards, Springer, New-York, pp. 23-97.

Ciz, R., Shapiro, S. A., 2007. Generalization of Gassmann equations for porous media saturated with a solid material. Geophysics 72, A75-A79.

Cumming, W., Bruhn, D., 2010. Preface. Geothermics 39, 1-3.

Eberhart-Phillips, D., 1986. Three-dimensional velocity structure in the northern California coast ranges from inversion of local earthquake arrival times. Bull. Seismol. Soc. Am. 76, 1025–1052.

Eberhart-Phillips, D., 1990. Three-dimensional P and S velocity structure in the Coalinga region, California. J. Geophys. Res. 95, 15343–15363.

Eberhart-Phillips, D., 1993. Local earthquake tomography: earthquake source region, In: Iyer, H.M., and Hihara K.(Editors), Seismic Tomography: Theory and

Practice, Chapman and Hall, London, U.K., pp. 613–643.

Eberhart-Phillips, D., Michael, A. J., 1998. Seismotectonics of the Loma Prieta, California, region determined from three-dimensional V_P, V_P/V_S, and seismicity. J. Geophys. Res. 103 (B9), 21099–21120.

Eberhart-Phillips, D., and Reyners, M., 1997. Continental subduction and three-dimensional crustal structure: The northern South Island, New Zealand. J. Geophys. Res. 102 (B6), 11,843–11,861.

Elders, W. A., and Fridleifsson, G. O., 2010. The Science Program of the Iceland Deep Drilling Project (IDDP): a study of supercritical geothermal resources. In: Proceedings World Geothermal Congress 2010, Bali, Indonesia, 25-29 April 2010, 9 pp.

Ellsworth, W. L., Eberhart-Phillips, D., Kissling, E., 1991. A test of local earthquake tomography. Seism. Res. Lett. 62, 31-32.

Evans, J. R., Eberthart-Phillips, D., and Thurber, C. H., 1994. User's manual for SIMULPS12 for imaging V_P and V_P/V_S: a derivative of the "Thurber" tomographic inversion SIMUL3 for local earthquakes and explosions. Open-file report, 94-431, United States Geological Survey, Washington, DC, USA, Open-file report, 94-431, 101 pp.

Evans, J. R., Foulger, G. R., Julian, B. R., Miller, A., 1996. Crustal shear-wave splitting from the local earthquakes in the Hengill triple junction, southwest Iceland. Geophys. Res. Lett. 23 (5), 455–458.

Faust, L. 1953. A velocity function, including lithologic variation. Geophysics 18, 271–288.

Feigl, K., Gasperi, G., Sigmundsson, F., Rigo, A., 2000. Crustal deformation near Hengill volcano, Iceland 1993-1998: coupling between magmatic activity and faulting inferred from elastic modelling of satellite radar interferrograms. J. Geophys. Res. 105, 25655–25670.

Foulger, G. R., 1988a. The Hengill triple junction, SW Iceland: 1. tectonic structure and the spatial and temporal distribution of local earthquakes. J. Geophys. Res. 93, 13493–13506.

Foulger, G. R. 1988b. The Hengill triple junction, SW Iceland: 2. anomalous earthquake focal mechanisms and implications for process within the geothermal reservoir and at accretionary plate boundaries. J. Geophys. Res. 93, 13507–13523.

Foulger, G. R., 1995. The Hengill geothermal area, Iceland: variation of temperature gradients deduced from the maximum depth of seismogenesis. J. Volcanol. Geotherm. Res. 65, 119–133.

Foulger, G. R. and Long, R., 1984. Anomalous focal mechanism solutions: evidence for tensile crack formation on an accretionary plate boundaries. Nature 310, 43–

45.

Foulger, G.. R., Long, R., Einarsson, P., E., and Björnsson, A., 1989. Implosive earthquakes at the active accretionary plate boundary in Iceland. Nature 337, 640–642.

Foulger, G. R., Miller, A., Julian, B., Evans, J., 1995. Three-dimensional V_P and V_P/V_S, structure of the Hengill Triple Junction and geothermal area, Iceland, and the repeatability of tomographic inversion. Geophys. Res. Lett. 22(10),1309–1312.

Foulger, G. R., and Toomey, D., 1989. Structure and evolution of the Hengill-Grendalur central volcano complex, Iceland: geology, geophysics and seismic tomography. J. Geophys. Res. 94, 17511–17522.

Fournier, R. O., 1999. Hydrothermal processes related to movement of fluid from plastic into brittle rock in the magmatic-epithermal environment. Economic Geology 94 (8), 1193-1211.

Frantz, J. D., Marshall, W. L., 1984. Electrical conductances and ionization constants of salts, acids and bases in supercritical aqueous fluids: 1. hydrochloric acid from 100°C to 700°C and at pressures to 4000 bars. Am. Journ. Sci. 284, 651-667.

Franzson, H., Gunnlaugsson, E., Arnason, K., Saemundsson, K., Steingrimsson, B., Hardarson, B. S., 2010. The Hengill geothermal system, conceptual model and thermal evolution. In: Proceedings World Geothermal Congress 2010, Bali, Indonesia, 25-29 April 2010, 9 pp.

Fridleifsson, G. O., Elders, W. A., 2005. The Iceland Deep Drilling Project: a search for deep unconventional geothermal resources. Geophysics 34(3), 269–285.

Gassmann, F., 1951. Über die elastizität poröser medien. Veirteljahrschrift der Naturforschenden Gesellschaft in Zürich 96,1–23.

Geoffroy, L., Dorbath, C., 2008. Deep downward fluid percolation driven by localized crust dilatation. Geophys. Res. Lett. 35, 1–6.

Golub, G. H., Reinsch, C., 1971. Singular value decomposition and least squares solutions. In: Handbook for Automatic Computation, II Linear Algebra, J.H. Wilkinson and C. Reinsch (Editors), Springer-Verlag, New-York, pp. 134–151.

Gudmundsson, B. T., Arnórson, S., 2002. Geochemical monitoring of the Krafla and Námafjall geothermal areas, N-Iceland. Geothermics 31, 195–243.

Gunasekera, R., Foulger, G., and Julian, B., 2003. Reservoir depletion at the Geysers geothermal area, california, shown by four-dimensional seismic tomography. J. Geophys. Res. 108(B3), 559–583.

Gunnarsson, A., Steingrimsson, B., Gunnlaugsson, E., Magnusson, J., and Maack, R., 1992. Nessjavellir geothermal co-generation power plant. Geothermics 21 (4), 559–583.

Gunnarsson, G., Arnaldsson, A., and Oddsdottir, A. L., 2010. Model simulation of the geothermal fields in the Hengill area, south-western Iceland. In: Proceedings World Geothermal Congress 2010, Bali, Indonesia, 25-29 April 2010, 7 pp.

Halladay, N., Deltombe, J.-L., Naisse, J.-M., Johnston, C., Lebert, F., Asmundsson, R., 2010. Borehole instruments for supercritical geothermal reservoirs. In: Proceedings World Geothermal Congress 2010, Bali, Indonesia, 25-29 April 2010, 5 pp.

Haraldsdottir, S. H., Franzson, H., Arnason, K., Einarsson, G. M., Bjornsson, H., 2010. Comparison of down-hole and surface resistivity data from the Hellisheidi geothermal field, SW Iceland. In: Proceedings World Geothermal Congress, Bali, Indonesia, 25-29 April 2010, 7 pp.

Hardarson, B., Einarsson, G. M., Kritsjánsson, B. R., Gunnarsson, G., Helgadóttir, H. M., Franzson, H., Arnason, K., Agutsson, K., Gunnlaugsson, E., 2010. Geothermal reinjection at the Hengill Tripple Juncion, SW Iceland. In: Proceedings World Geothermal Congress, Bali, Indonesia, 25-29 April 2010, 7 pp.

Harris, P., MacGregor, L., 2006. Determination of reservoir properties from the integration od CSEM and seismic data. First Break 24, 15–21.

Humphreys, E., Clayton, R. W., 1988. Adaptation of back projection tomography to seismic travel time problems. J. Geophys. Res. 93, 4731–4735.

Husen, S., Kissling, E., Flueh, E., Ash, G., 1999. Accurate hypocentre determination in the Seismogenic Zone of the subducting Nazca plate in the northern Chile using a combined on/off-shore network. Geophys. J. Int. 138, 687–701.

Husen, S., Smith, R. B., and Waite, G.P., 2004. Evidence for gas and magmatic sources beneath the Yellowstone volcanic field from seismic tomographic imaging. J. Volcanol. Geotherm. Res. 131, 397–410.

Ingolfsson, O., Sigmarsson, O., Sigmundsson, F., Símonarson, L., 2008. The dynamic geology of Iceland. Jökull 58, 1–2.

Iyer, H. M., Hirahara, K. (Editors), 1993. Seismic Tomography: Theory and Practice. Chapman and Hall, London, U.K., 847 pp.

Jakobsdóttir, S., 2008. Seismicity in Iceland. Jökull 58, 75–100.

Jaya, M. S., Shapiro, S. A., Krinstindóttir, L. H., Bruhn, D., Milsh, H., Spangenberg, E., 2010. Temperature dependence of seismic properties in geothermal rocks at reservoir conditions. Geothermics 39(1), 113–123.

Jolly, A., Sherburn, S., Jousset, P., and Kilgour, G., 2010. Eruption source processes derived from seismic and acoustic observations of the 25 September 2007 Ruapehu eruption, North Island, New Zealand. J. Volcanol. and Geotherm. Res. 191, 33–45.

Jousset, P. 2006. Sismologie large bande: méthodologie et applications: apport en géothermie haute enthalpie à Bouillante, Guadeloupe. Report BRGM RP-54701-FR, BRGM, Orléans, France, 119 pp.

Jousset, P., Bitri, A., Loiseau, J., Bouchot, V., 2010a. Seismic ambient noise study at Bouillante geothermal system, French Antilles. In: Geophysical Research Abstracts, EGU General Assembly 2010, p. EGU2010–5305.

Jousset, P., Francois, B., 2006. Set-up of a broadband seismological network at Hengill geothermal field (Iceland). Report BRGM RP-54971-FR, BRGM, Orléans, France, 51 pp.

Jousset, P., Haberland, C., Bauer, K., Arnason, K., Weber, M., Fabriol, H., 2010b. Seismic tomography and long-period earthquakes observation and modelling at the Hengill geothermal system. In: Proceedings World Geothermal Congress, Bali, Indonesia, 25-29 April 2010, 7 pp.

Jousset, P., Neuberg, J., Jolly, A., 2004. Modelling low-frequency earthquakes in a viscoelastic medium with topography. Geophys. J. Int. 159, 776–802.

Jousset, P., Neuberg, J., Sturton, S., 2003. Modelling the time-dependent frequency content of low-frequency volcanic earthquakes. J. Volcanol. and Geotherm. Res. 128, 201–223.

Julian, B. R., Miller, A., Foulger, G. R., 1997. Non-double couple earthquake mechanisms at the Hengill-Grensdalur volcanic complex. Geophys. Res. Lett. 24 (7), 743–746.

Kissling, E., 1988. Geotomography with local earthquake data. Rev. Geophys. 26, 659–698.

Kissling, E., Ellsworth, W., Eberhart-Phillips, D., Kradolfer, U., 1994. Initial reference models in local earthquake tomography. J. Geophys. Res. 99, 19635–19646.

Koulakov, I., Bohm, M., Asch, G., Luehr, B.-G., Manzanares, A., Brotopuspito, K. S., Fauzi, P., Purbawinata, M. A., Puspito, N. T., Ratdomopurbo, A., Kopp, H., Rabbel, W., Shevkunova, E., 2007. P and S velocity structure of the crust and the upper mantle beneath central Java from local tomography inversion. J. Geophys. Res. 112, B08310, doi 10.1029/2006JB004712.

Kristinsdóttir, L. H., Flóvenz, O., Arnason, K., Bruhn, D., Milsh, H., Spangenberg, E., Kulenkampff, J., 2010. Electrical conductivity and P-wave velocity in rock samples from high-temperature Icelandic geothermal fields. Geothermics 39, 94-105.

Kummerow, J., 2005. The influence of intergrannular, supercritical water on the elastic properties of rocks. PhD thesis, Freien Universität Berlin, Berlin, Germany, 119 pp.

Lebert, F., Asmundsson, R., 2009. High temperature instrumentation in geothermal

fields at supercritical conditions of reservoirs fluid. In: Workshop on Devices for harsh environments. Material, Processing, Characterisation, Vienna, June 2009. Institute of Sensor and Actuators systems and 4M network of Excellence, Vienna, Austria. 4 pp.

Lees, J. M., Crosson, R. S., 1989. Tomographic inversion for three-dimensional velocity structure at Mount St. Helens using earthquake data. J. Geophys. Res. 94, 5716–5728.

Leonard, M., Kennett, B., 1999. Multi-component autoregressive techniques for the analysis of seismograms. Phys. Earth. Planet. Interiors 113, 247–264.

Maeda, N. 1985. A method for reading and checking phase times in auto-processing system of seismic wave data. Zizin, 38, 365–379.

Majer, E. L., Baria, R., Stark, M., Oates, S., Bommer, J., Smith, B., Asanuma, H., 2007. Induced seismicity associated with Enhanced Geothermal Systems. Geothermics 36, 185–222.

Michelini, A., 1993. Testing the reliability of V_P/V_S anomalies in travel time tomography. Geophys. J. Int. 114, 405–410.

Miller, A., Julian, B., Foulger, G. R., 1998. Three-dimensional seismic structure and moment tensors of non-double couple earthquakes at the Hengill-Grensdalur volcanic complex, Iceland. Geophys. J. Int. 133, 309–325.

Milsch, H., Kristinsdóttir, L. H., Spangenberg, E., Bruhn, D., Flóvenz, O., 2010. Effect of the water-steam phase transition on the electrical conductivity of porous rocks. Geothermics 39, 106-114.

Mogi, K., 1958. Relations between the eruptions of various volcanoes and the deformations of the ground surfaces around them. Bull. Earthq. Res. Inst. Univ. Tokyo 36, 99–134.

Munoz, G., Bauer, K., Moeck, I., Schulze, A., Ritter, O., 2010. Exploring the gross schönebeck (Germany) geotehrmal site using a statistical joint interpretation of magnetotelluric and seismic tomography models. Geothermics 39 (1), 35–45.

Newman, G., Gasperikova, E., Hoevrsten, G., Wanamaker, P., 2008. Three-dimensional magnetotelluric characterization of the Coso geothermal field. Geothermics 37, 369–399.

Palmer, D.A., Fernandez-Prini, R., Harvey, A.H., 2004 (Editors). Aqueous systems at elevated temperatures and pressures; Physical chemistry in water, steam and hydrothermal solutions., Elsevier Ltd., Oxford, U.K., 745 pp.

Pavlis, G. L., Booker, J. R., 1980. The mixed discrete-continuous inverse problem: application to the simultaneous determination of earthquake hypocentres and velocity structure. J. Geophys. Res. 85, 4801–4810.

Pedersen, R., Sigmundsson, F., Einarsson, P., 2007. Controlling factors on earthquake

swarms associated with magmatic intrusions; contraints from Iceland. J. Volcanol. Geotherm. Res. 162, 73–80.

Pitzer, K. S., 1983. Dielectric constant of water at very high temperature and pressure, Proc. Natl. Acad. Sci. 80, 4575-4576.

Ragnarsson, A., 2010. Geothermal development in Iceland 2005-2009. In: Proceedings World Geothermal Congress 2010, Bali Indonesia, 25-29 April 2010, 11 pp.

Roeker, S. W., 1982. Velocity structure of the Pamir-Hindu Kush region: possible evidence of subducted crust. J. Geophys. Res. 87, 945–959.

Saemundsson, K., 1995. Hengill, Jardhiti, Ummyndun og Grunnvatn, 1:25000 (Hengill, Geothermal, Alteration and Groundwater). Orkustofunun, Reykjavik, Iceland.

Sens-Schönfelder, C., Korn, M., Stefánsson, R., 2006. Joint interpretation of the size and time distributions of seismic activity around the Hengill triple junction (SW Iceland) between 1993 and 1996. J. Seismol. B7, 15151–15161. doi 10.1007/s10950-006-9011-5

Sigmundsson, F., Einarsson, P., Rögnvaldsson, S. T., Foulger, G. R., Hodgkinson, K. M., Thorbergsson, G., 1997. The 1994-1995 seismicity and deformation at the hengill triple junction, Iceland: triggering of earthquakes by minor magma injection in a zone of horizontal shear stress. J. Geophys. Res. 102 (B7), 15151–15161.

Spencer, C., Gubbins, D., 1980. Travel-time inversion for simultaneous earthquake location and velocity structure determination in laterally varying media. Geophys. J. R. Astron. Soc. 63, 95–116.

Stefánsson, R., Bödvarsson, R., Slunga, R., Einarsson, P., Jakobsdóttir, S., Bungum, H., Gregersen, S., Havskov, J., Hjelme, J., and Korhonen, H., 1993. Earthquake prediction research in the South Iceland Seismic Zone and the SIL Project. Bull. Seismol. Soc. Am. 83, 696–716.

Stimac, J. A., Goff, F., Counce, D., Larocque, A. C. L., Hilton, D. R., Morgenstern, U., 2003. The crater lake and hydrothermal system of Mount Pinatubo, Philippinnes: evolution in the decade after the eruption. Bulletin of Volcanology 66 (2), 149-167.

Tester, J. W., Anderson, B., Batchelor, A., Blackwell, D., DiPippo, R., Drake, E., Garnish, J., Livesay, B., Moore, M.C., Nichols, K., Petty, S., Toksoz, N., Veatch, R., Augustine, C., Baria, R., Murphy, E., Negraru, P., Richards, M. 2006. The future of geothermal energy: Impact of enhanced geothermal systems (EGS) on the United States in the 21st century. Massachusetts Institute of Technology, Cambridge, Massachusetts, USA,, 209 pp.

Thurber, C. H., 1983. Earthquake locations and three-dimensional crustal structure in the Coyote Lake area, central California. J. Geophys. Res. 88 (B10), 8226–8236.

Thurber, C. H., 1986. Analysis methods for kinematic data from local earthquakes. Rev. Geophys. 24, 793–805.

Thurber, C. H., 1993. Local earthquake tomography: velocities and V_P/V_S-theory. In: Iyer, H.M, Hihara K.(Editors), Seismic Tomography: Theory and Practice. Chapman and Hall, London, U.K., pp. 563–583.

Toomey, D. R., Foulger, G. R., 1989. Application of tomographic inversion to local earthquake data from the Hengill-Grendalur central volcano complex, Iceland. Phys. Earth and Plan. Int. 94, 17497–17510.

Tryggvason, A., Rögnvaldsson, S. T., Flovenz, O. G., 2002. Three-dimensional imaging of the P and S-wave velocity structure and earthquake locations beneath Southwest Iceland. Geophys. J. Int. 151, 848–866.

Ussher, G. C., Harvey, C., Johnstone, R., Anderson, E., 2000. Understanding the resistivities observed in geothermal systems. In: Proceedings World Geothermal Congress 2000, Kyushu-Tohoku, Japan, pp. 1915-1920.

Wadati, K., 1933. On the travel-time of earthquake waves. Geophysical Magazine 7,101–111.

Ward, P. L., 1972. Microearthquakes: prospecting tool and possible hazard in the development of geothermal resources. Geothermics 1, 3–12.

Yao, Z. S., Roberts, R. G., and Tryggvason, A., 1999. Calculating resolution and covariance matrices for seismic tomography with the LSQR method. Geophys. J. Int. 138, 886–894.

Zhang, H., Thurber, C., Rowe, C., 2003. Automatic P-wave arrival detection and picking with multiscale wavelet analysis for single-component recordings. Bull. Seismol. Soc. Am. 93 (5), 1904–1912.

Appendix: Parametrization for the tomography

The arrival time of a seismic wave from an earthquake at a station is a nonlinear function of the earthquake location, which includes its spatial coordinates , the earthquake origin time τ, and the velocity structure along the wave path (Thurber, 1983). According to ray theory (e.g., Aki and Richards, 2002), the nonlinear functional relationship can be written as:

$$t = \tau + \int_{l[u(\mathbf{r})]} u(\mathbf{r}) dl \qquad (A.1)$$

where τ is the arrival time, $u(\mathbf{r})$ is the slowness or reciprocal of velocity, dl is the differential length along the ray, and $l[u(r)]$ is the ray path, a function of the earthquake hypocentre and velocity structure along the ray path. For a pair (earthquake i, receiver j), linearisation of Eq.(A.1) about a starting model and earthquake location results in the equation:

$$r_{ij} = \sum_{k=1}^{3} \frac{\partial T_{ij}}{\partial x_k} \Delta x_k + \Delta \tau_i + \int_{\text{ray-path}} \delta u(\mathbf{r}) dl \qquad \text{(A.2)}$$

where r_{ij} is the arrival time residual, T_{ij} is the travel time from the i^{th} earthquake to the j^{th} station, $\frac{\partial T_{ij}}{\partial x_k}$ are the partial derivatives of travel time with respect to the spatial coordinates, Δx_k and $\Delta \tau_i$ are perturbations to the starting earthquake hypocentre, and $\delta u(r)$ is the slowness perturbation to the reference model. The arrival time residual is the difference between the observed arrival time and the theoretical arrival times based on the starting earthquake location and the reference velocity model.

The parametrization of the structural reference model may take several forms (Thurber, 1993; Koulakov et al., 2007). The most commonly used approach is to define a uniform or nonuniform grid of constant slowness cells (Benz et al., 1996). When the reference model is parametrized as a uniform grid of constant slowness cells, the system of equations may be written in a matrix form (Tryggvason et al., 2002):

$$\begin{bmatrix} \gamma_i^P \\ \gamma_i^S \end{bmatrix} = \begin{bmatrix} A_i^P & B_i^P & 0 \\ A_i^S & 0 & B_i^S \end{bmatrix} \begin{bmatrix} \Delta h_i \\ \Delta u^P \\ \Delta u^S \end{bmatrix} \qquad \text{(A.3)}$$

where A_i is the matrix of partial derivatives of travel times with respect to hypocentre location, Δh_i is the vector of hypocentre perturbations, B_i is the matrix of distances travelled in each cell and Δu the vector of slowness perturbations. Superscript P and S are for the P– and S– waves respectively. The coupling between the P– and S– velocity models and the hypocentre locations in this equation is very clear. Accurate determination of the velocity structure requires a large number of sources, resulting in many unknowns. The solution of this system of equations makes use of the property

$$U_0^T A_i = 0 \qquad \text{(A.4)}$$

where U_0 are the eigenvectors associated with the zero singular values of $A_i A_i^T$ (Golub and Reinsch, 1971). This property allows the separation between slowness and hypocentre perturbations (Pavlis and Booker, 1980; Spencer and Gubbins, 1980). Model parametrization artifacts and solution instability may also be minimized using constraint equations (Lees and Crosson, 1989; Benz et al., 1996; Tryggvason et al., 2002).

List of Figures

Figure 1: Topographic map of Hengill Volcano, Iceland, with the location (large black triangles) of the broadband seismological stations (HE1, HE2, HE3, HE4, HE5, HE6, HE7) and SIL network stations (KRO, SAN, HEI). Stations of previous tomography by Foulger and Toomey (1989) are indicated by inverted grey triangles. Our station density is similar to that of previous studies. Small grey squares are locations of geothermal wells; they are grouped in three areas (Nesjavellir, Hellisheidi and Olkelduháls/Bitra). The three main volcanic centers are indicated in italics (Hengill, Hrómundartindur and Grensdalur). The inset map shows the location of Hengill volcano in Iceland.

Figure 2: Example of the picking technique using AIC criteria. The time window must be chosen to include the segment of seismogram of interest only. For a very clear P-wave onset in the seismogram, AIC values have a very clear global minimum at the sample where the P-wave is thought to begin. For a low signal to noise ratio, the global minimum does not give satisfactory results.

Figure 3: Statistics of the P-wave (top) and S-wave (bottom) arrival time picking for 343 volcano-tectonic earthquakes recorded by the IGET seismic network.

Figure 4: Wadati diagram for 324 volcano-tectonic earthquakes recorded at Hengill with the IGET seismic network. The slope is V_P/V_S = 1.765 +/- 0.122.

Figure 5: A 1D V_P model inverted from P- and S-waves arrival times. The top plot shows the inverted P-wave velocity, with the 50 lowest RMS models illustrated as light lines and the minimum as a heavy black line. The 1D velocity models from Toomey and Foulger (1989), Tryggvason et al. (2002) and Stefánsson et al. (1993) are shown for reference. The *a priori* locations of 339 earthquakes from the preliminary inversion are shown in map view in the middle plot and in cross-section in the right and bottom plots, oriented NS and WE, respectively. Seismic station locations are shown as black triangles, topography as dotted lines, and wells are grey squares. Horizontal and vertical scales are consistent.

Figure 6: Ray paths for each arrival observed at stations from the earthquake locations, shown in map view (top) and cross-section view (right NS and left WE).

Figure 7: Spread values for several horizontal slices at different depths. Dark shading (low spread values) in the center of the model volume indicates good resolution. The outer regions show reduced resolution as indicated by lighter shading. Circles are earthquake hypocentres in the neighbourhood (+/- 0.5 km) of the plane of the section. Seismic stations are represented in this figure with white triangles.

Figure 8: Spread values S-N and E-W cross-sections. Dark shading (low spread values) in the center of the model volume indicates good resolution. The outer regions show a reduced resolution as indicated by lighter shading. Small crosses represent locations of the inverted parameter V_P. Circles are earthquake hypocentres in the neighbourhood (+/- 0.05 degrees) of the plane of the section. Seismic stations are represented in this figure with black triangles at the free surface (black line).

Figure 9: Horizontal slices of the checkerboard test for the final grid inversion. Left plots show the initial model with perturbations of +/–5% of the 1D velocity model. Plots on the right show the result of the tomographic inversion of synthetic travel times computed for the perturbed model using the final earthquake location. The depths are shown to the right of the maps.

Figure 10: Vertical sections (E-W) of the checkerboard test for the final grid inversion. Left plots show the initial model with perturbations of +/–5% of the 1D velocity model. Plots on the right show the result of the tomographic inversion of synthetic travel times computed for the perturbed model using the final earthquake location. The latitudes are shown to the right of the sections.

Figure 11: Vertical sections (SN) of the checkerboard test for the final grid inversion. Left plots show the initial model with perturbations of +/–5% of the 1D velocity model. Plots on the right show the result of the tomographic inversion of synthetic travel times computed for the perturbed model using the final earthquake location. The longitudes are shown to the right of the sections.

Figure 12: Maps comparing P-wave velocity patterns from 3D inversions using grid spacings of 2 km (top row), 1.5 km (center row) and 1 km (bottom row) at depths indicated at the top of each column. Small crosses are V_P grid nodes. Black triangles are station locations, and white circles are earthquake locations within +/-500 m of the map depth. Dashed lines are 100 m topographic contours. The small grey squares are geothermal well heads. Little red stars indicate surface hydrothermal features. The locations of the cross-sections in Figure 16 are shown in the bottom row of maps.

Figure 13: Cross-sections comparing P-wave velocity patterns in 3D inversions using grid spacings of 2 km (top row), 1.5 km (middle row) and 1 km (bottom row). Section orientation is in a S-N direction at left and W-E direction at right. See Figure 12 for symbol descriptions in the caption and line-of-section in the bottom row of maps in Figure 12.

Figure 14: Cross-sections comparing P-wave velocity 3D anomalies using a grid spacing of 1 km. Section orientation is in a S-N direction at left and in W-E direction at right. See Figure 12 for symbol descriptions in the caption and line-of-section in the bottom line of maps.

Figure 15: Maps comparing V_P/V_S ratio patterns from 3D inversion using a grid spacing of 1 km, at depths indicated at the lower left corner of each map. Small crosses are grid nodes, black triangles are station locations, and white circles are earthquake locations within +/-500 m of the map depth. Dashed lines are 100 m topographic contours. The small grey squares are locations of geothermal well-heads. Little red stars indicate surface hydrothermal features. The locations of the cross-sections in Figures 16 are shown in all maps as black lines.

Figure 16: Cross-sections comparing V_P/V_S ratio patterns in 3D inversions using grid spacing of 1 km. Section orientation is in the S-N direction at the left and in the W-E direction at the right. See Figure 15 for symbol descriptions in the caption. Lines indicating the line-of-section are plotted in all maps.

Figure 17: Maps comparing tomographic V_P (left column), V_P/V_S (middle column) and resistivity (right column) models at 2.3 km (top row), 2.9 km (middle row) and 3.5 km depth (bottom row). In the resistivity maps, thick black lines indicate inferred faults at depth from long-term seismicity (Árnason et al., 2010). Dashed lines are 100 m topographic contours. Little red stars indicate surface hydrothermal features. The locations of the cross-sections in Figures 14 and 16 are shown in all maps as black lines.

Figure 18: Two-parameter histogram of log(resistivity) versus V_P/V_S. Higher density, that is, larger numbers of occurences in each range of log(resistivity) and V_P/V_S, are indicated with warm colors (reddish colors). The classes are defined in the text and in Table 1.

Figure 19: Interpreted maps at depths 2.3 km, 2.9 km and 3.5 km , after classes of V_P/V_S ratio/resistivity clusters have been defined from Figure 18. Black triangles represent seismic station locations. White circles are earthquake locations within +/- 500 m of the map depth. The number indicated in the corner left of each slice indicates the slice depth. Little stars indicate the hydrothermal features on ground surface.

Figure 20: Schematic model of Hengill geothermal system. Crosses are hypocentres.

Table 1: Classes defined in the cross-plot of the V_P/V_S ratio and log resistivity (Figure 18). The right column indicates the minimal number of instances in the cross-plot for each class.

Class	V_P/V_S ratio	log resistivity ρ	instances
1	$1.755 < V_P/V_S < 1.760$	$3.9<\log(\rho)<4.4$	>50
2	$1.765 < V_P/V_S < 1.775$	$3.3<\log(\rho)<3.8$	>45
3	$1.742 < V_P/V_S < 1.755$	$3.3<\log(\rho)<3.7$	>30
4	$1.752 < V_P/V_S < 1.760$	$2.8<\log(\rho)<3.1$	>40
5	$1.742 < V_P/V_S < 1.752$	$2.1<\log(\rho)<2.5$	>40
6	$1.764 < V_P/V_S < 1.777$	$2.3<\log(\rho)<2.7$	>55
7	$1.752 < V_P/V_S < 1.761$	$1.0<\log(\rho)<1.8$	>40
8	$1.765 < V_P/V_S < 1.771$	$0.2<\log(\rho)<0.7$	>50
9	$1.771 < V_P/V_S < 1.775$	$0.0<\log(\rho)<0.2$	>35

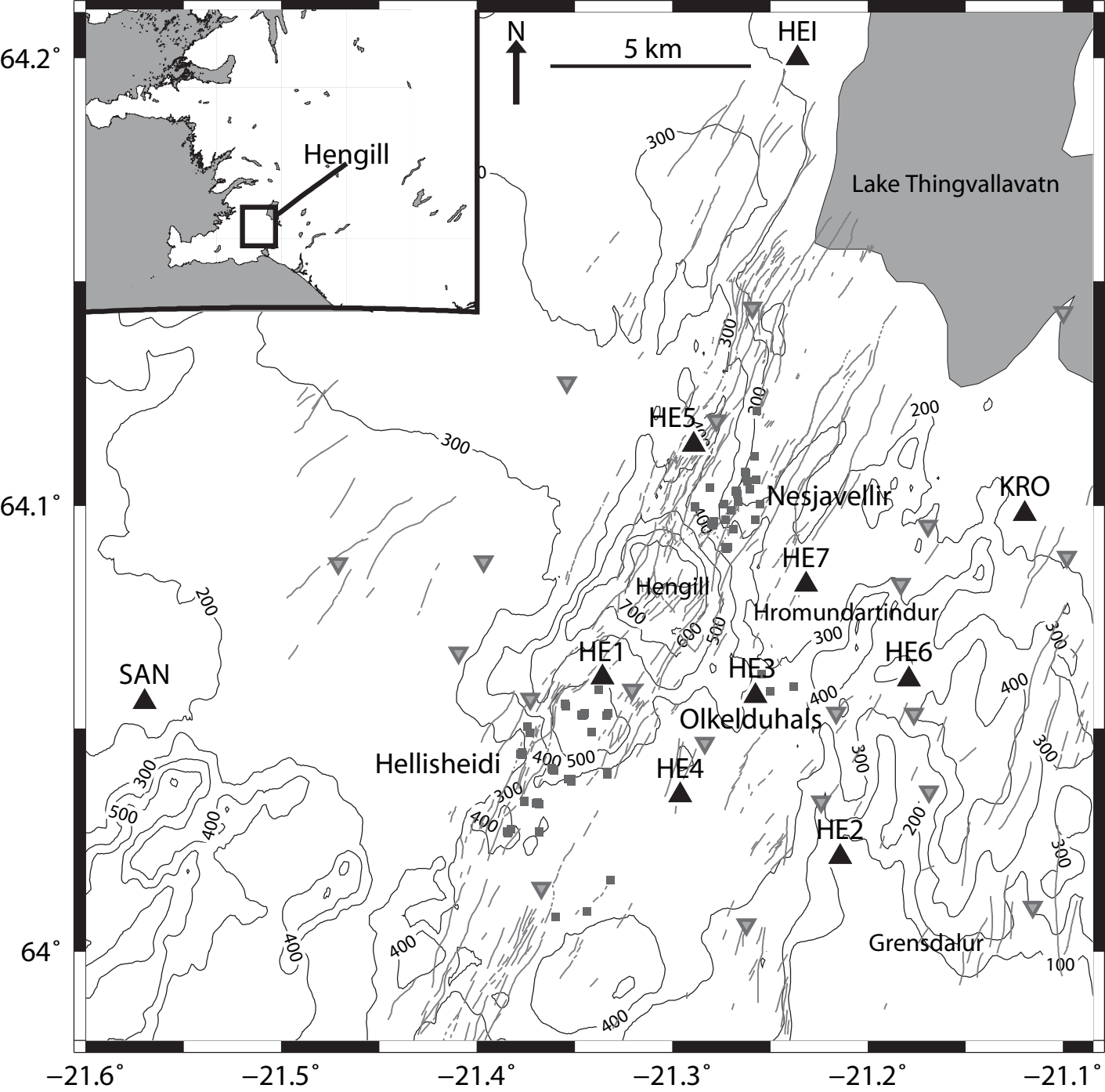
N
5 km
HEI
Hengill
Lake Thingvallavatn
HE5
Nesjavellir
KRO
HE7
Hengill
Hromundartindur
HE1
HE3
HE6
SAN
Olkelduhals
Hellisheidi
HE4
HE2
Grensdalur
64.2°
64.1°
64°
−21.6°
−21.5°
−21.4°
−21.3°
−21.2°
−21.1°

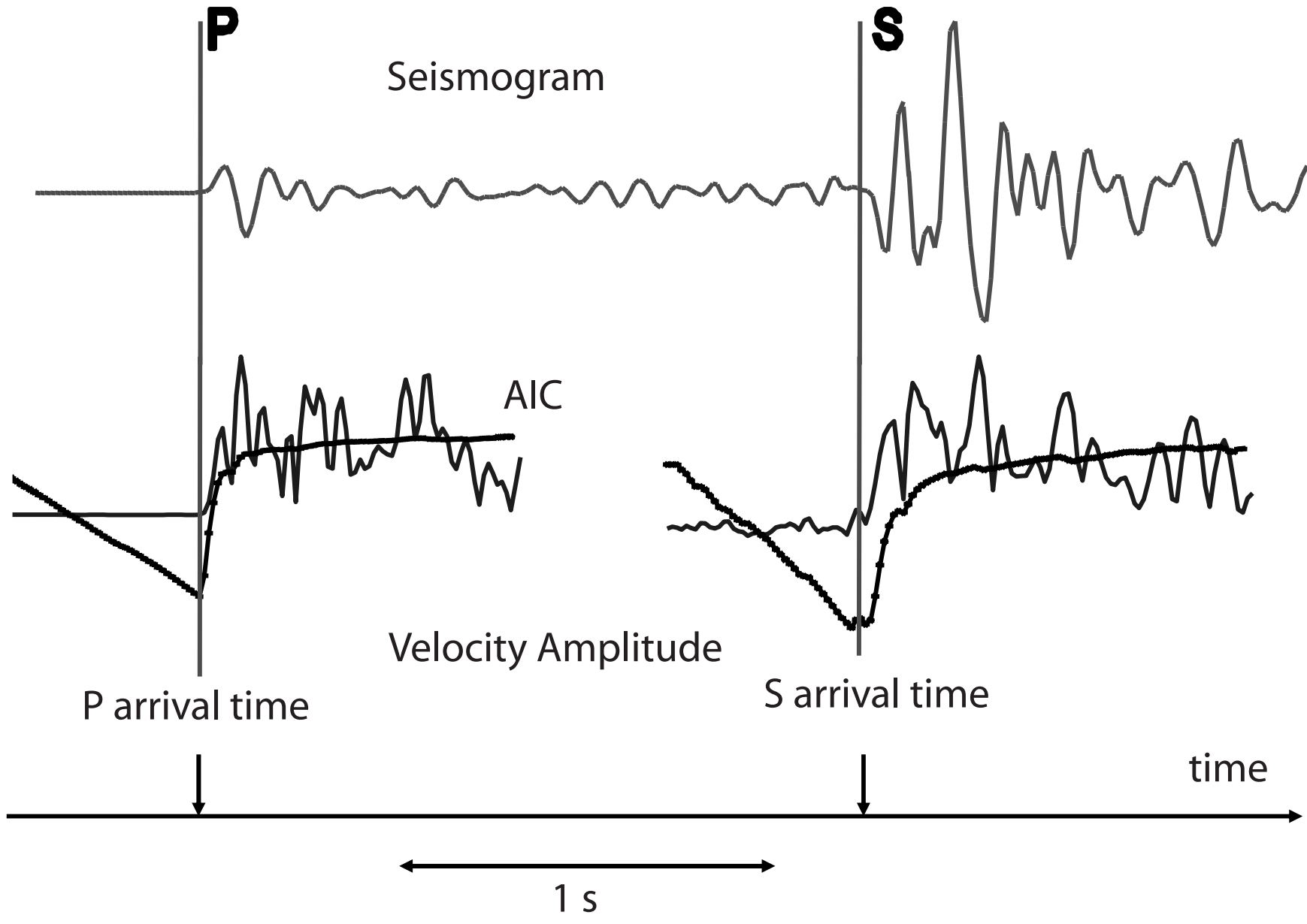
P
S
Seismogram
AIC
Velocity Amplitude
P arrival time
S arrival time
time
1 s

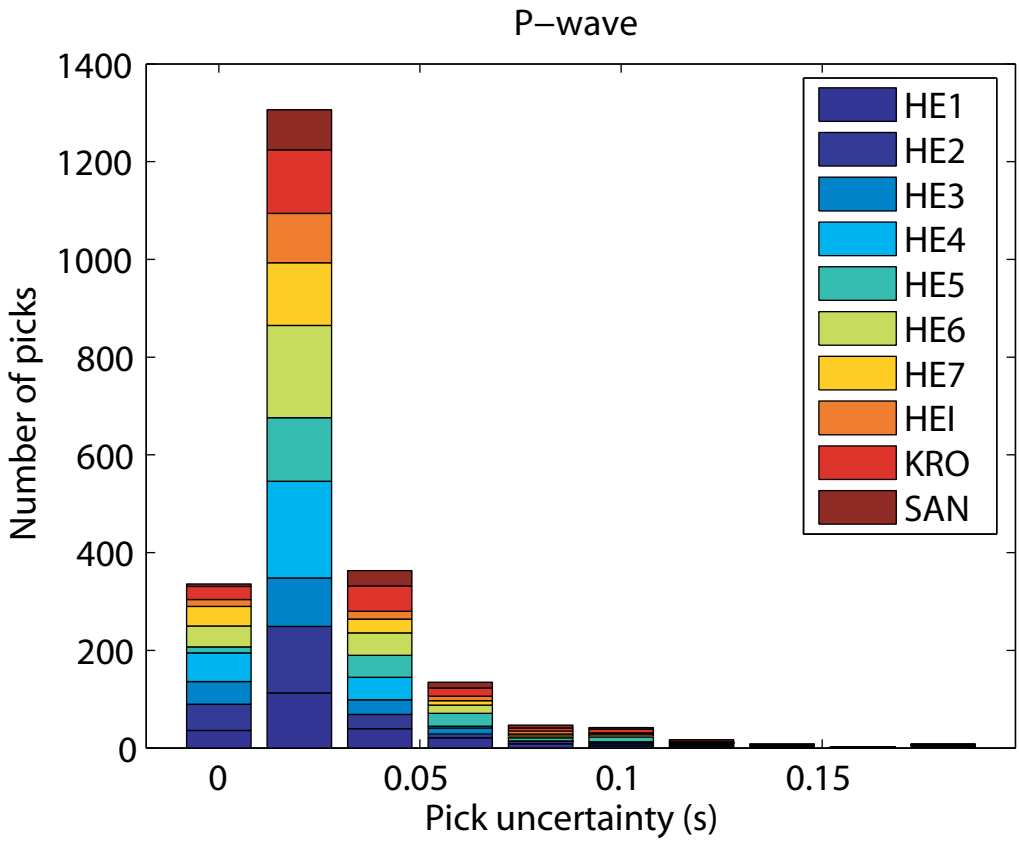
P–wave
1400
1200
1000
800
600
400
200
0
Number of picks
0
0.05
0.1
0.15
Pick uncertainty (s)
HE1
HE2
HE3
HE4
HE5
HE6
HE7
HEI
KRO
SAN

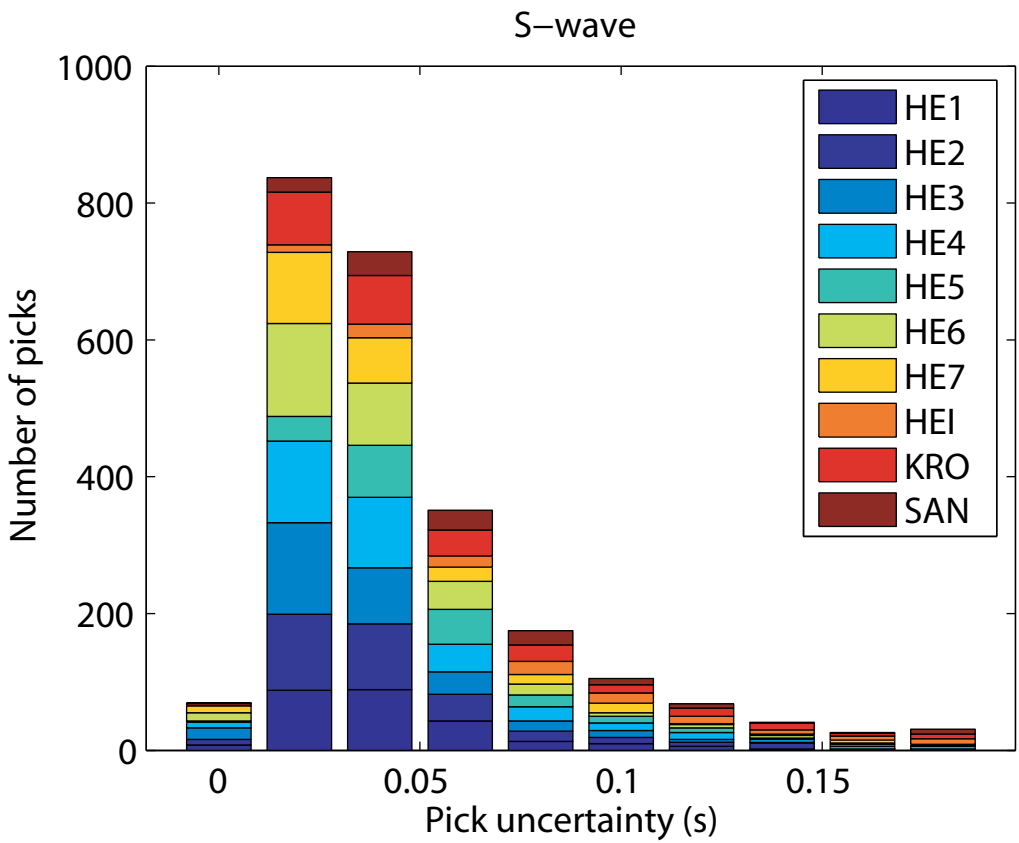
S–wave
1000
800
600
400
200
0
Number of picks
0
0.05
0.1
0.15
Pick uncertainty (s)
HE1
HE2
HE3
HE4
HE5
HE6
HE7
HEI
KRO
SAN

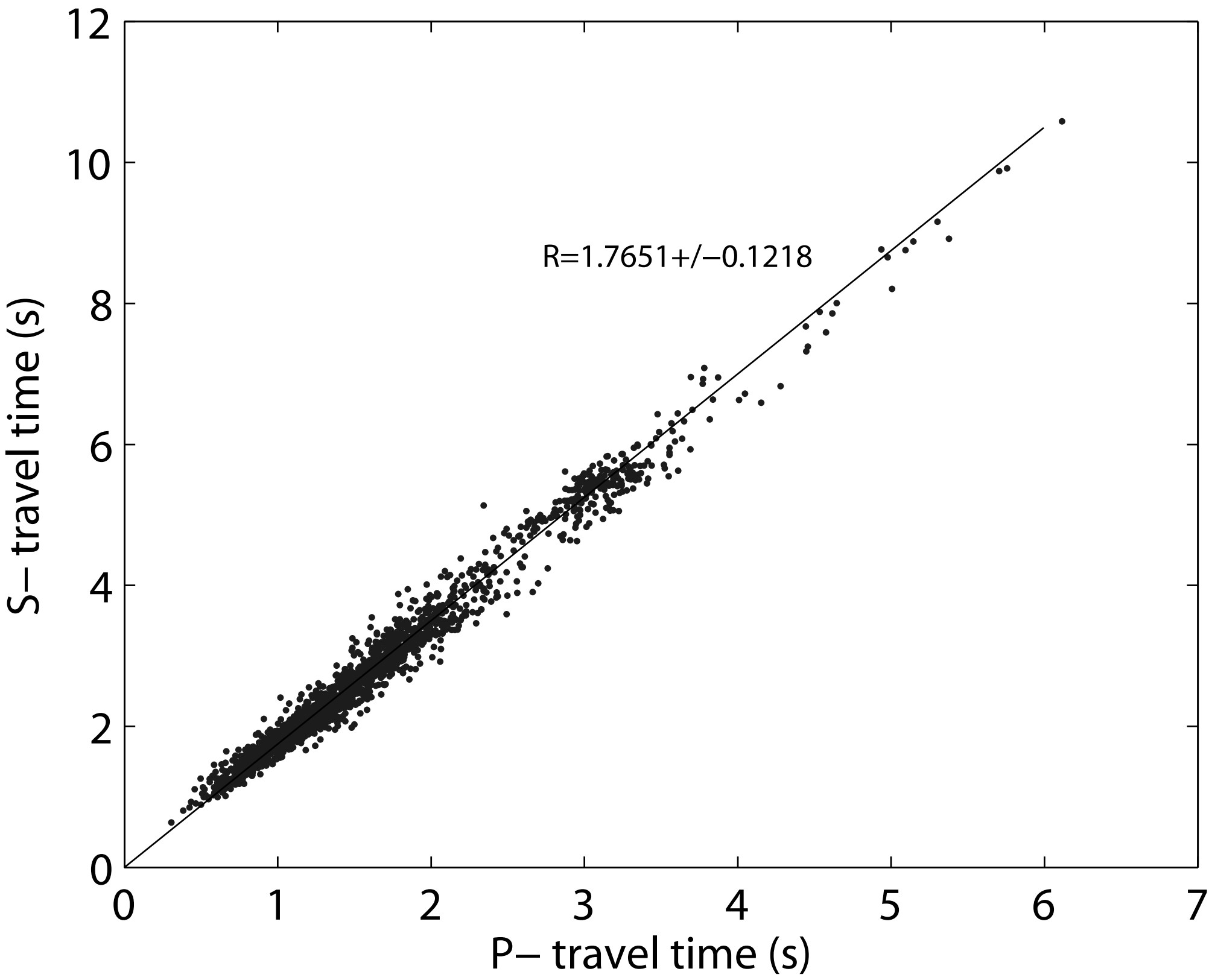
R=1.7651+/−0.1218
S− travel time (s)
P− travel time (s)
0
2
4
6
8
10
12
0
1
2
3
4
5
6
7

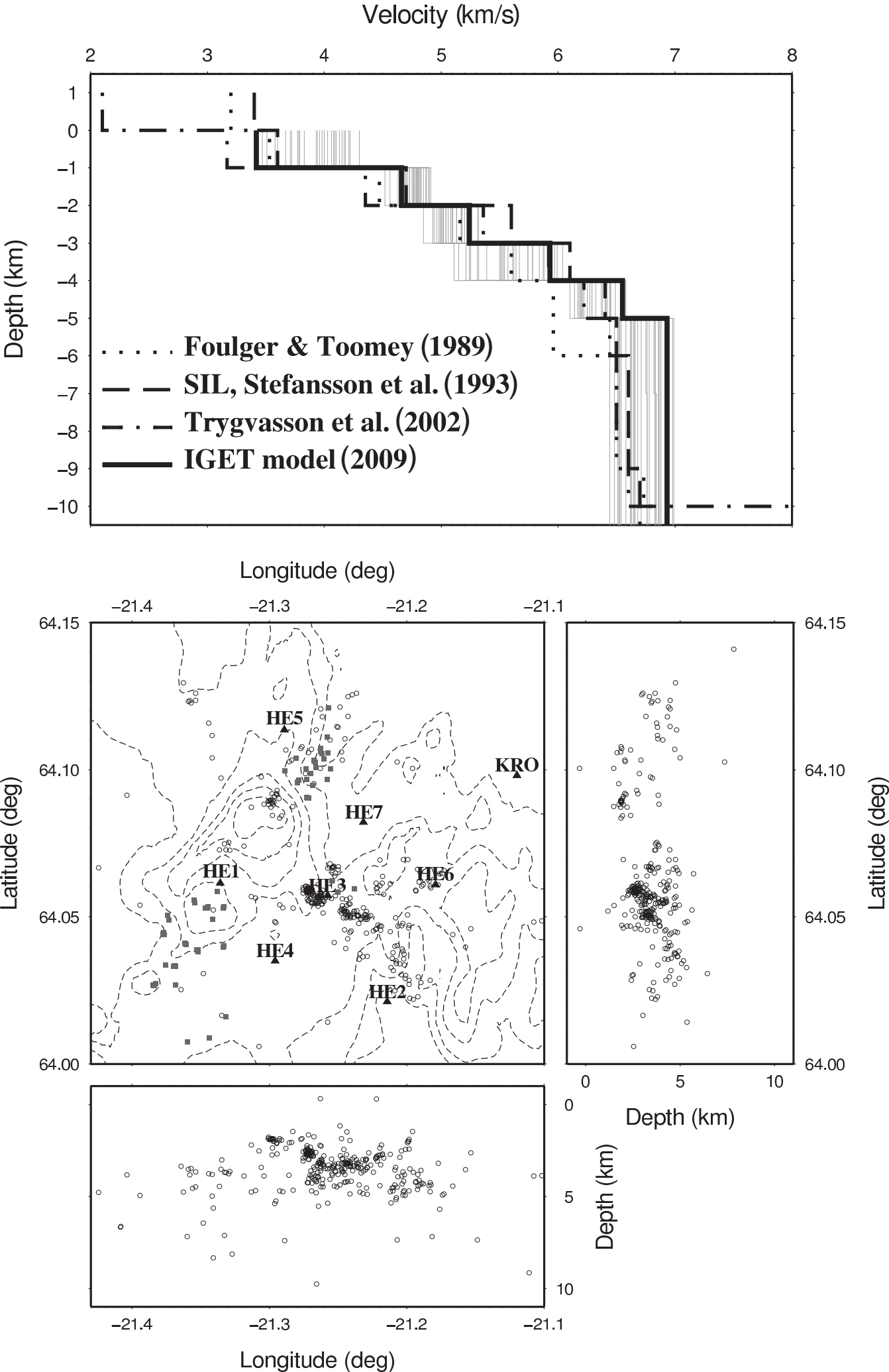
Velocity (km/s)
Depth (km)
Foulger & Toomey (1989)
SIL, Stefansson et al. (1993)
Trygvasson et al. (2002)
IGET model (2009)
Longitude (deg)
Latitude (deg)
HE5
KRO
HE7
HE1
HE3
HE6
HE4
HE2
Depth (km)

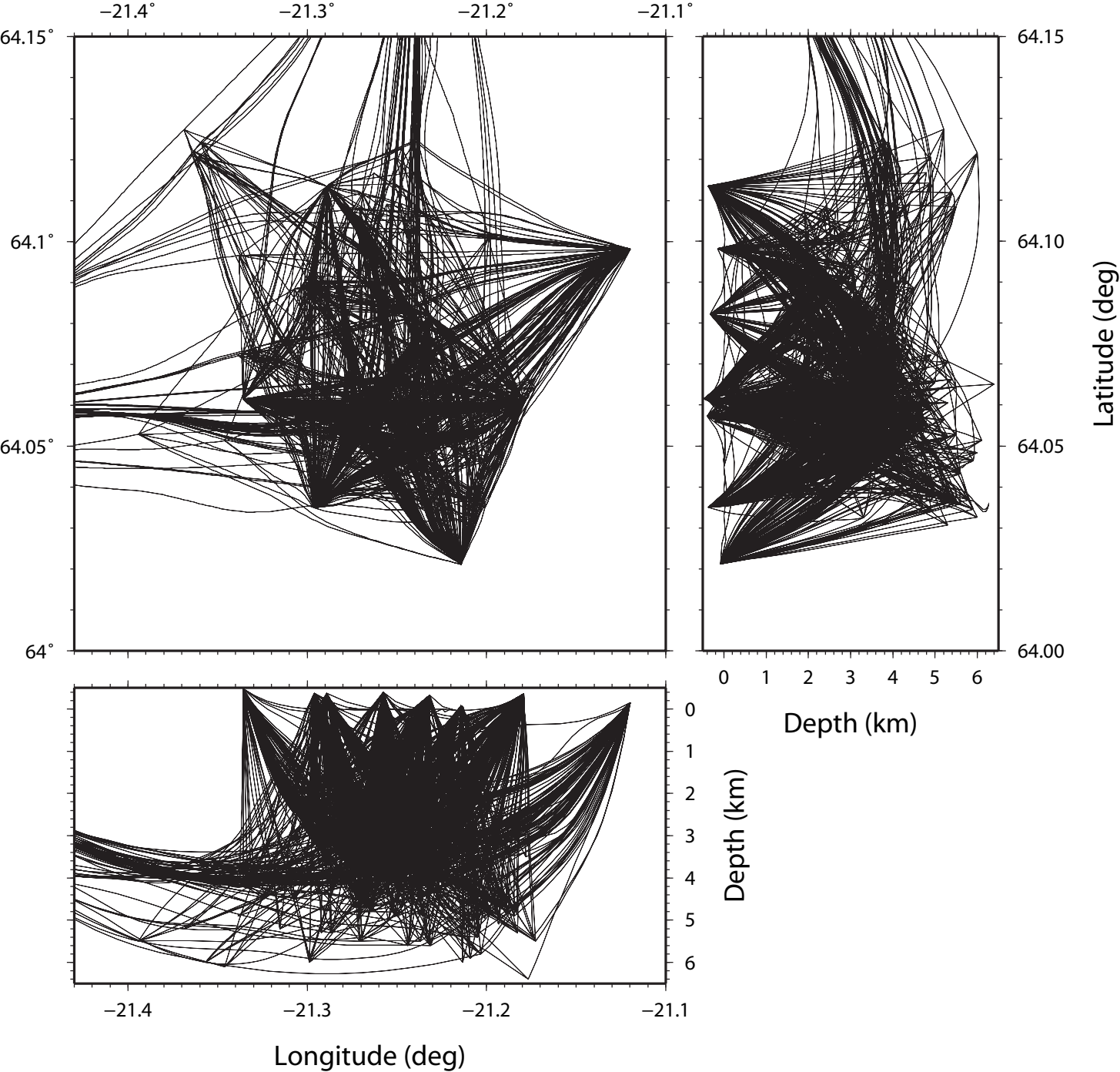
−21.4°
−21.3°
−21.2°
−21.1°
64.15°
64.1°
64.05°
64°
64.15
64.10
64.05
64.00
Latitude (deg)
0
1
2
3
4
5
6
Depth (km)
Depth (km)
−21.4
−21.3
−21.2
−21.1
Longitude (deg)

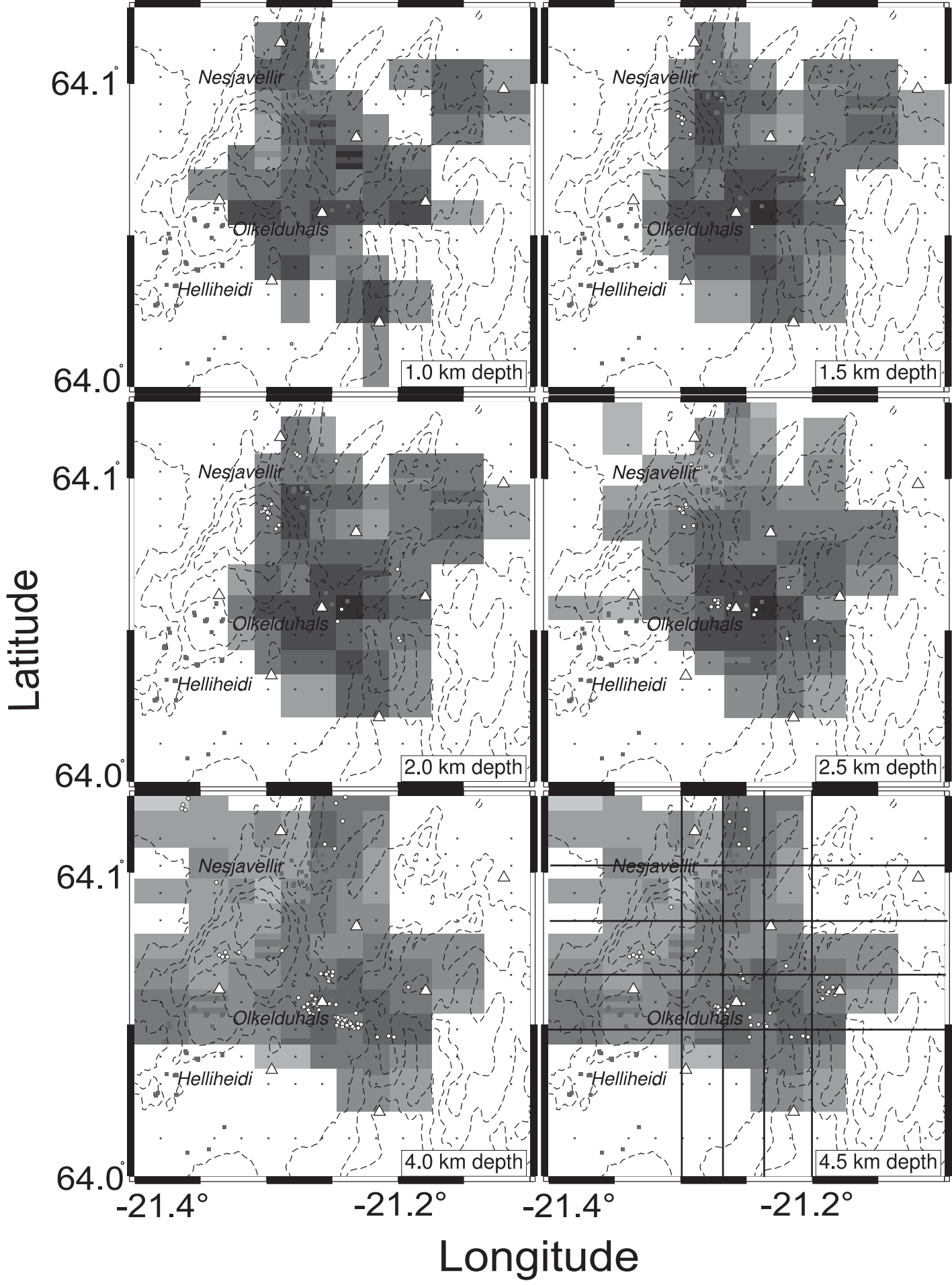
Nesjavellir
Olkelduhals
Helliheidi
1.0 km depth
1.5 km depth
2.0 km depth
2.5 km depth
4.0 km depth
4.5 km depth
64.1°
64.0°
-21.4°
-21.2°
Latitude
Longitude

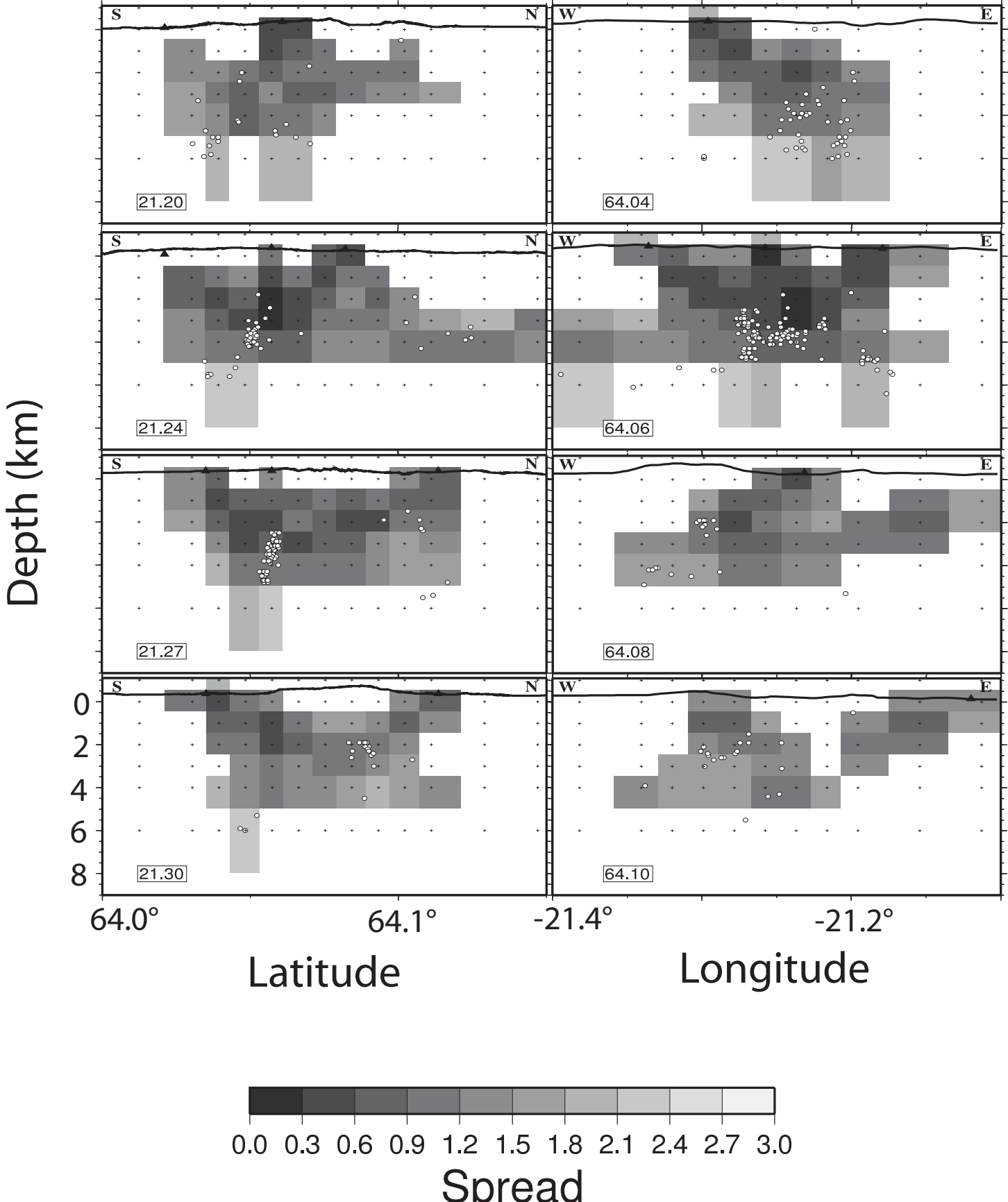
S
N
W
E
21.20
64.04
21.24
64.06
21.27
64.08
21.30
64.10
Depth (km)
0
2
4
6
8
64.0°
64.1°
-21.4°
-21.2°
Latitude
Longitude
0.0 0.3 0.6 0.9 1.2 1.5 1.8 2.1 2.4 2.7 3.0
Spread

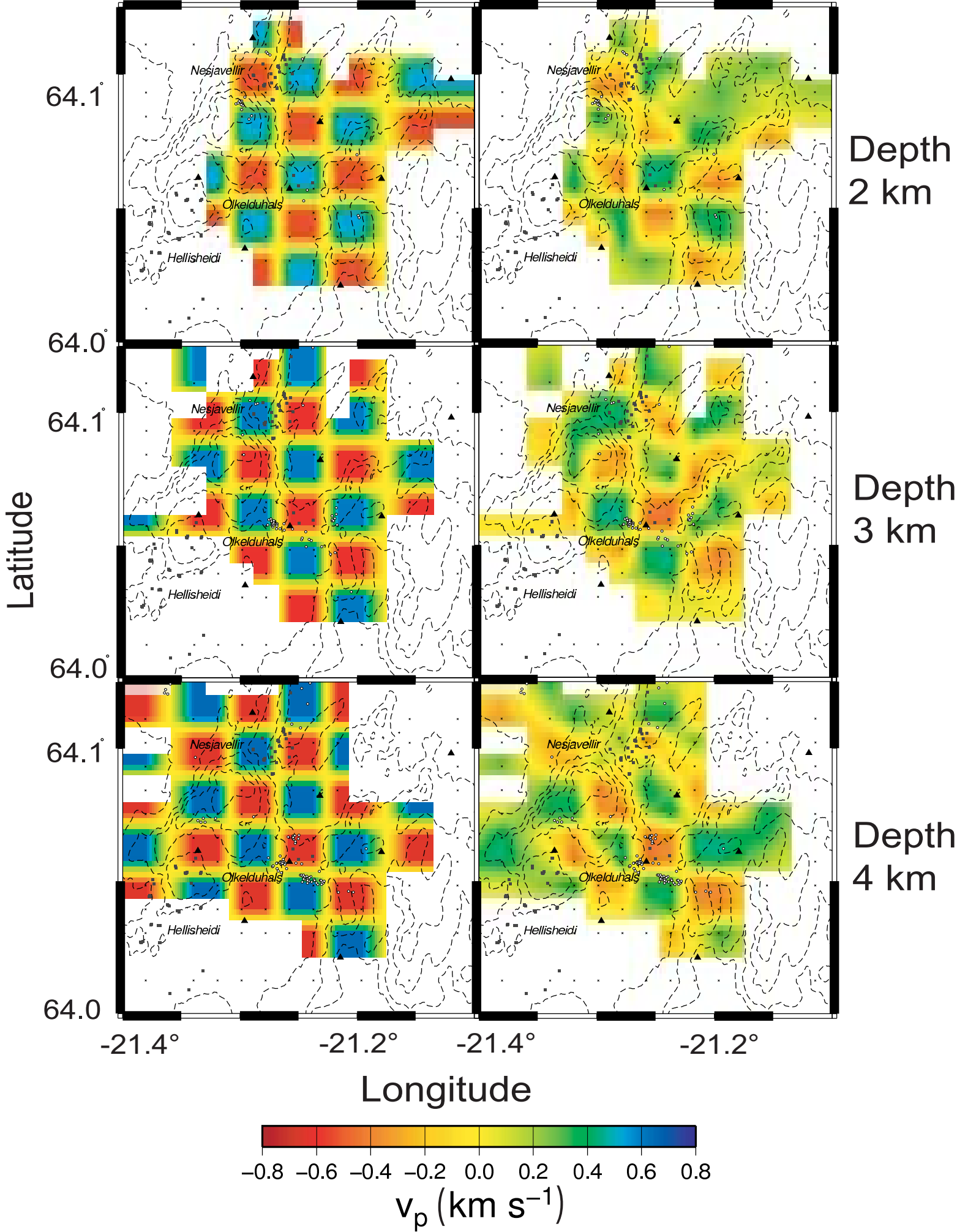
Nesjavellir
Ölkelduhals
Hellisheidi
64.1°
64.0°
Depth
2 km
Depth
3 km
Depth
4 km
Latitude
-21.4°
-21.2°
Longitude
−0.8 −0.6 −0.4 −0.2 0.0 0.2 0.4 0.6 0.8
v_p (km s^{-1})

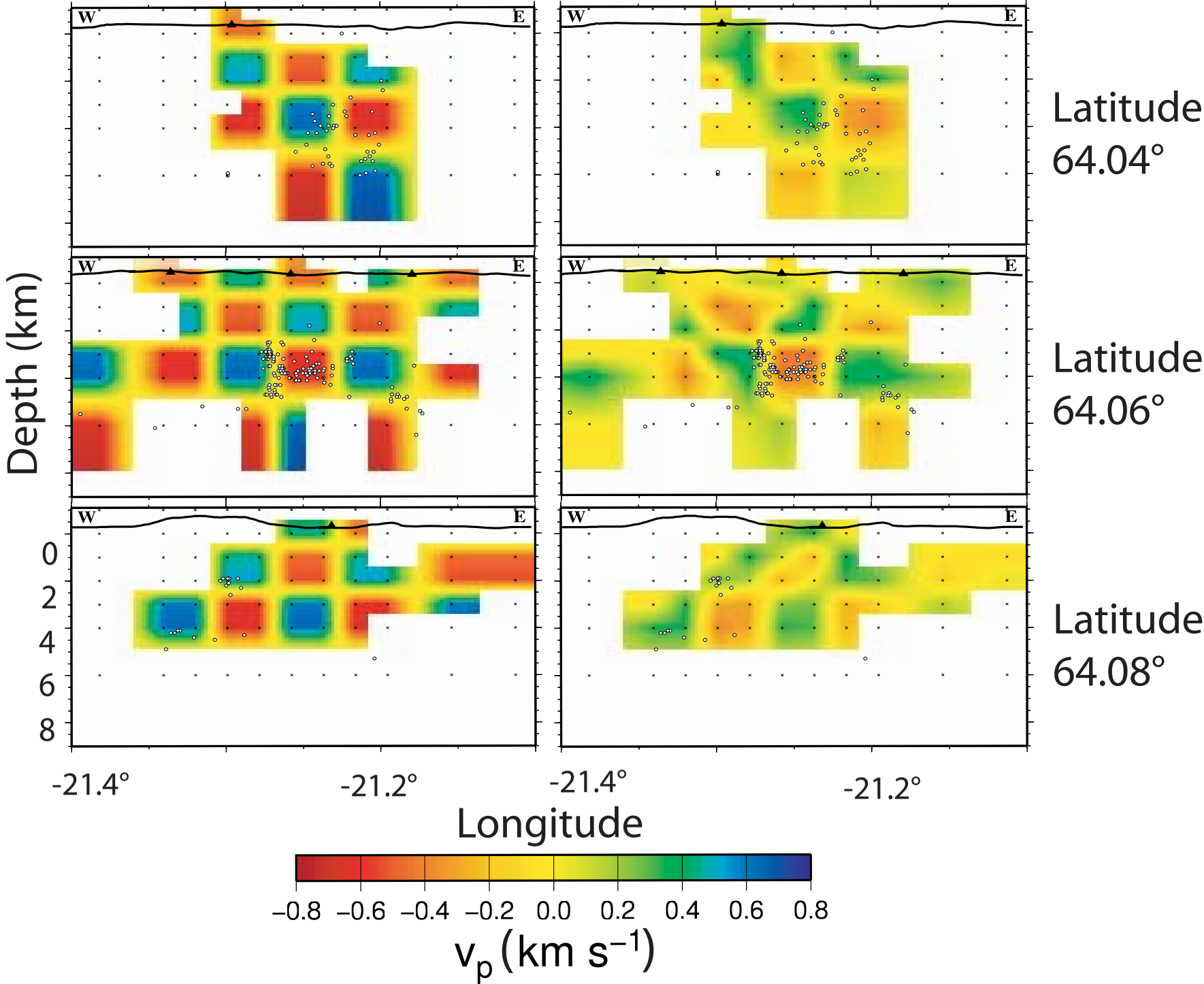
W
E
Latitude
64.04°
Latitude
64.06°
Latitude
64.08°
Depth (km)
0
2
4
6
8
-21.4°
-21.2°
-21.4°
-21.2°
Longitude
−0.8 −0.6 −0.4 −0.2 0.0 0.2 0.4 0.6 0.8
v_p (km s^{-1})

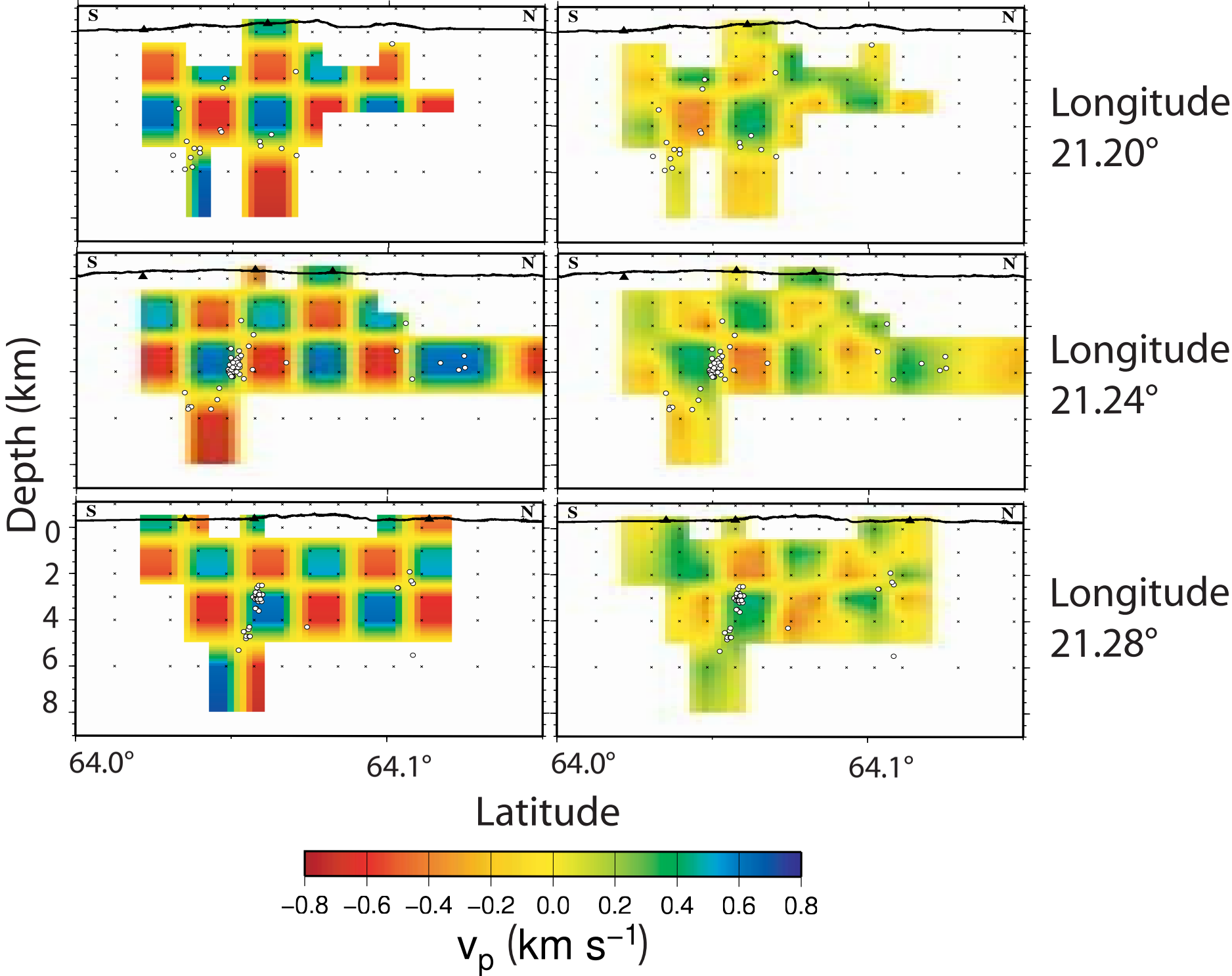
S
N
Longitude
21.20°
Longitude
21.24°
Longitude
21.28°
Depth (km)
0
2
4
6
8
64.0°
64.1°
64.0°
64.1°
Latitude
−0.8 −0.6 −0.4 −0.2 0.0 0.2 0.4 0.6 0.8
v_p (km s^{-1})

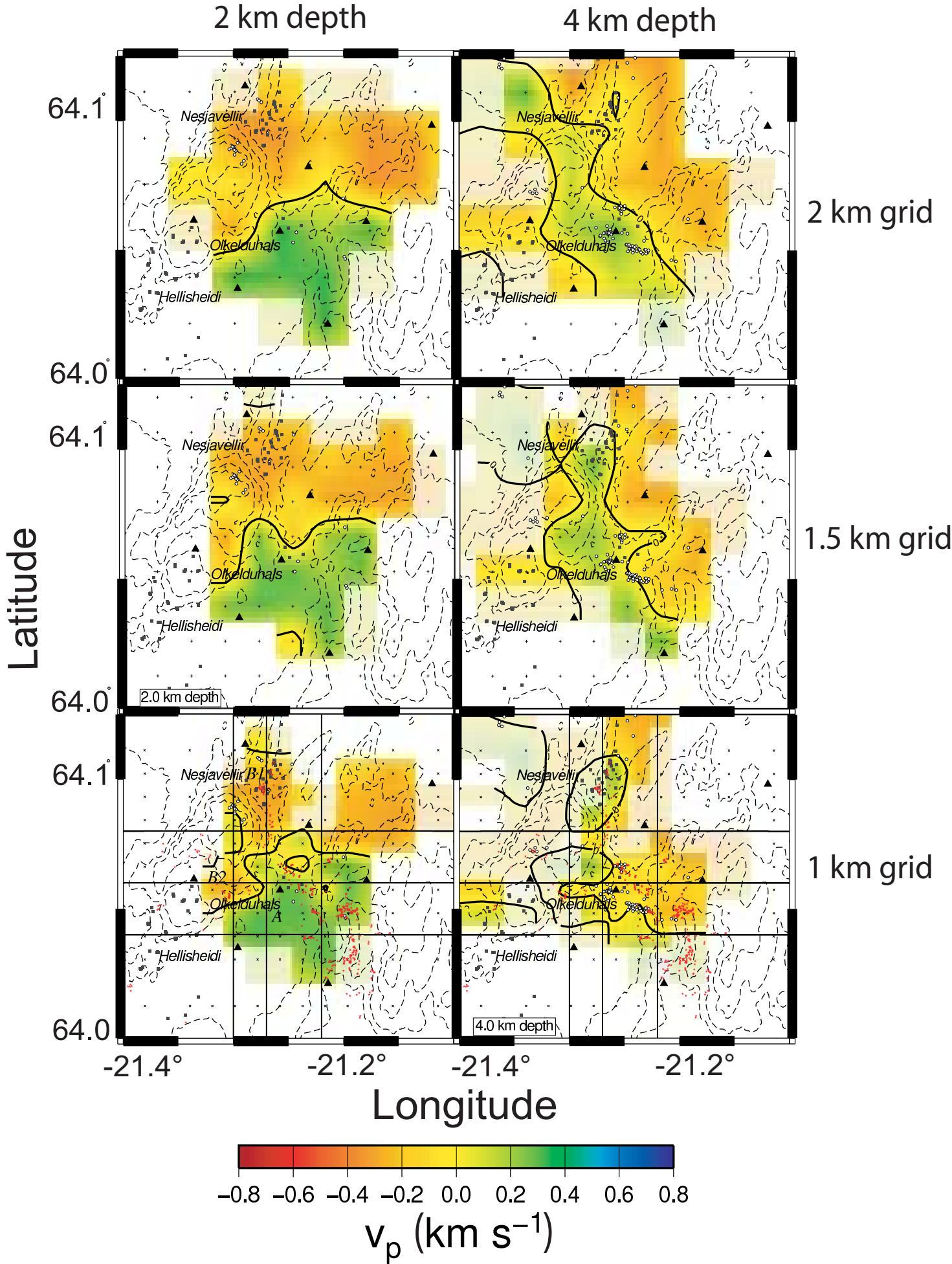
2 km depth
4 km depth
2 km grid
1.5 km grid
1 km grid
Latitude
Longitude
64.1°
64.0°
-21.4°
-21.2°
Nesjavellir
Olkelduhals
Hellisheidi
2.0 km depth
4.0 km depth
B1
B2
A
−0.8 −0.6 −0.4 −0.2 0.0 0.2 0.4 0.6 0.8
v_p (km s^{-1})

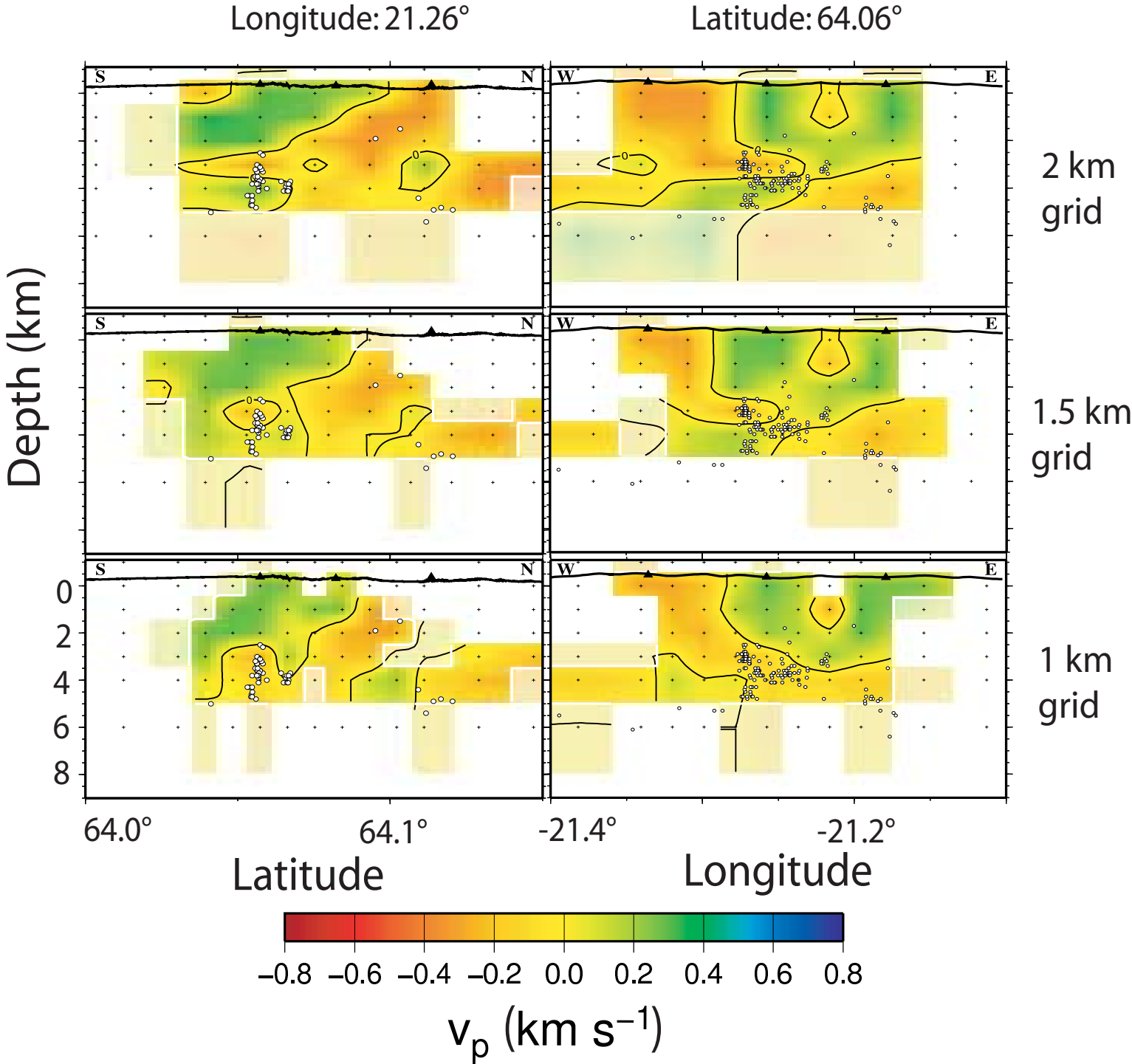
Longitude: 21.26°
Latitude: 64.06°
S
N
W
E
2 km grid
1.5 km grid
1 km grid
Depth (km)
0
2
4
6
8
64.0°
64.1°
Latitude
-21.4°
-21.2°
Longitude
–0.8 –0.6 –0.4 –0.2 0.0 0.2 0.4 0.6 0.8
v_p (km s^{-1})

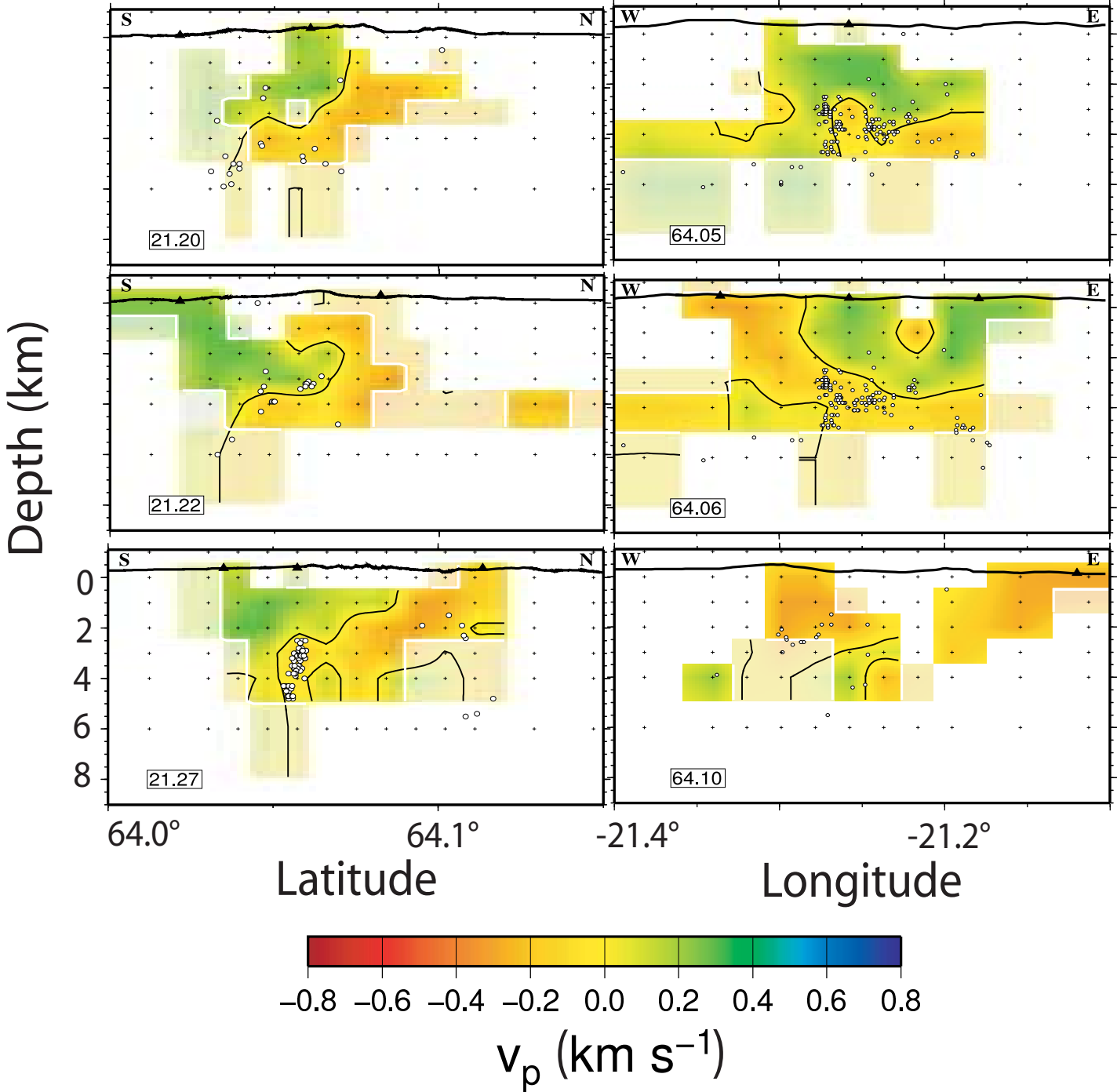
S
N
W
E
21.20
64.05
21.22
64.06
21.27
64.10
Depth (km)
0
2
4
6
8
64.0°
64.1°
-21.4°
-21.2°
Latitude
Longitude
–0.8 –0.6 –0.4 –0.2 0.0 0.2 0.4 0.6 0.8
v_p (km s^{-1})

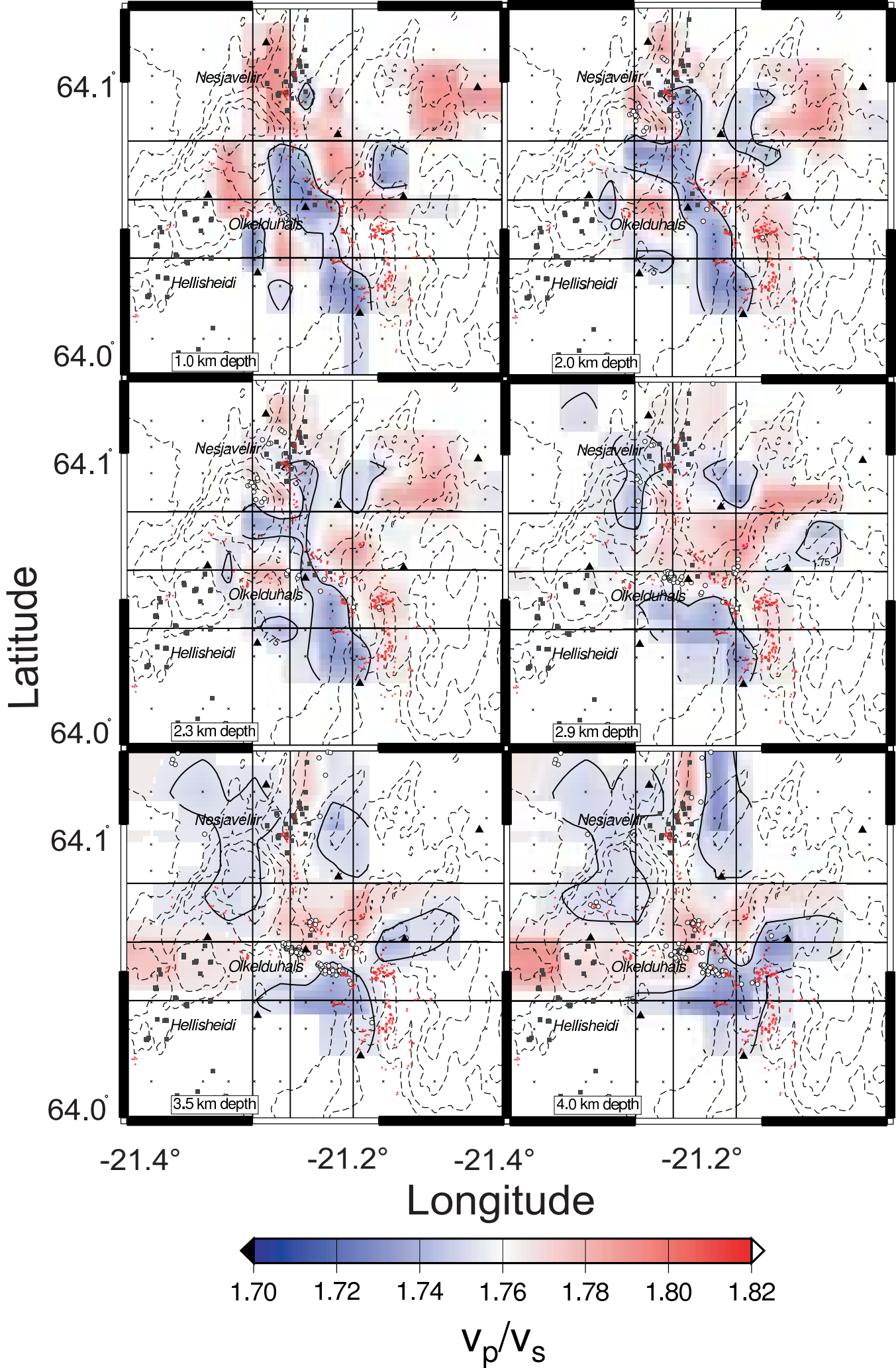
Nesjavellir
Olkelduhals
Hellisheidi
1.0 km depth
2.0 km depth
2.3 km depth
2.9 km depth
3.5 km depth
4.0 km depth
1.75
64.1°
64.0°
-21.4°
-21.2°
Latitude
Longitude
1.70
1.72
1.74
1.76
1.78
1.80
1.82
v_p/v_s

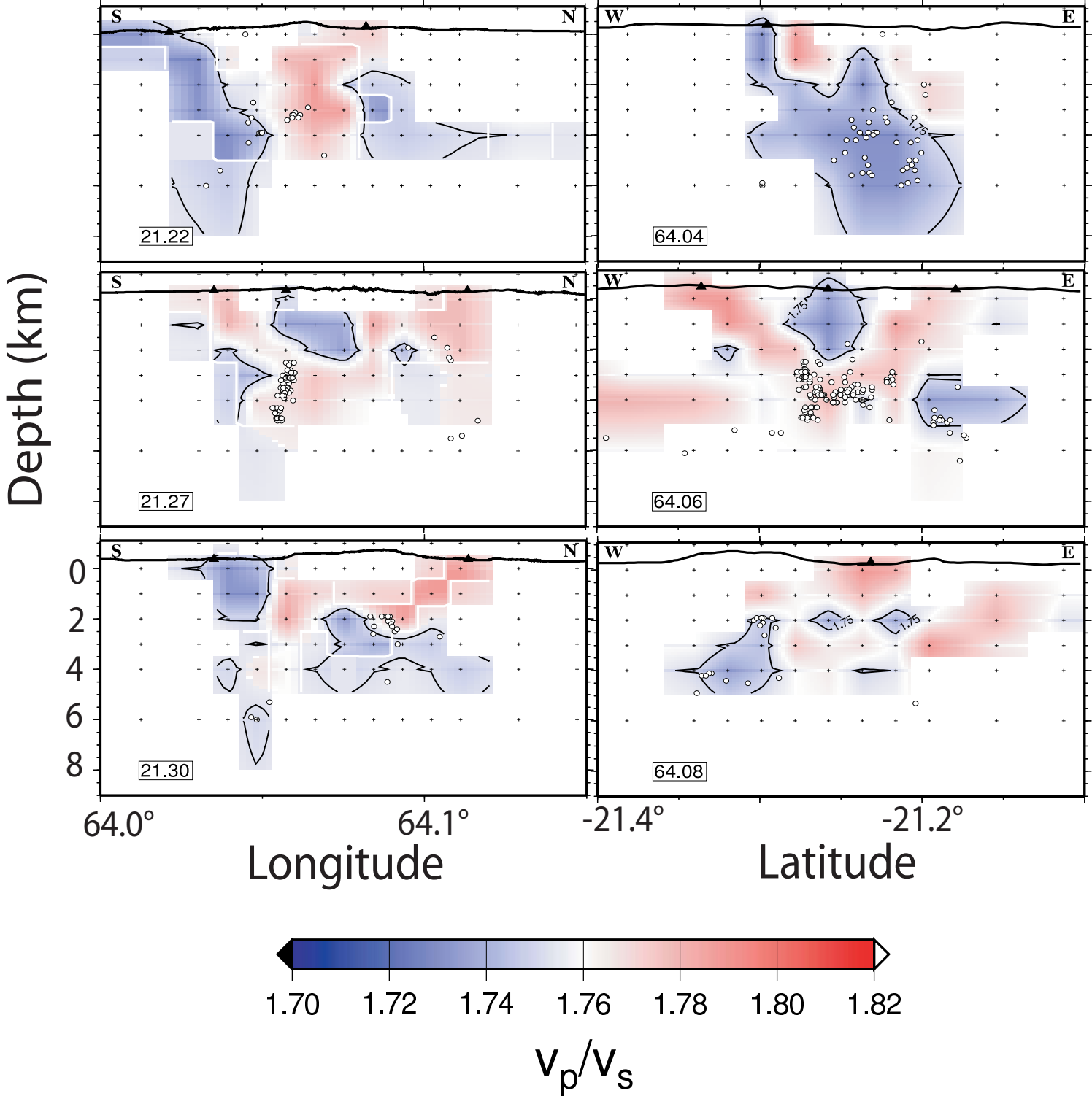
S
N
W
E
21.22
64.04
21.27
64.06
21.30
64.08
1.75
Depth (km)
0
2
4
6
8
64.0°
64.1°
-21.4°
-21.2°
Longitude
Latitude
1.70
1.72
1.74
1.76
1.78
1.80
1.82
v_p/v_s

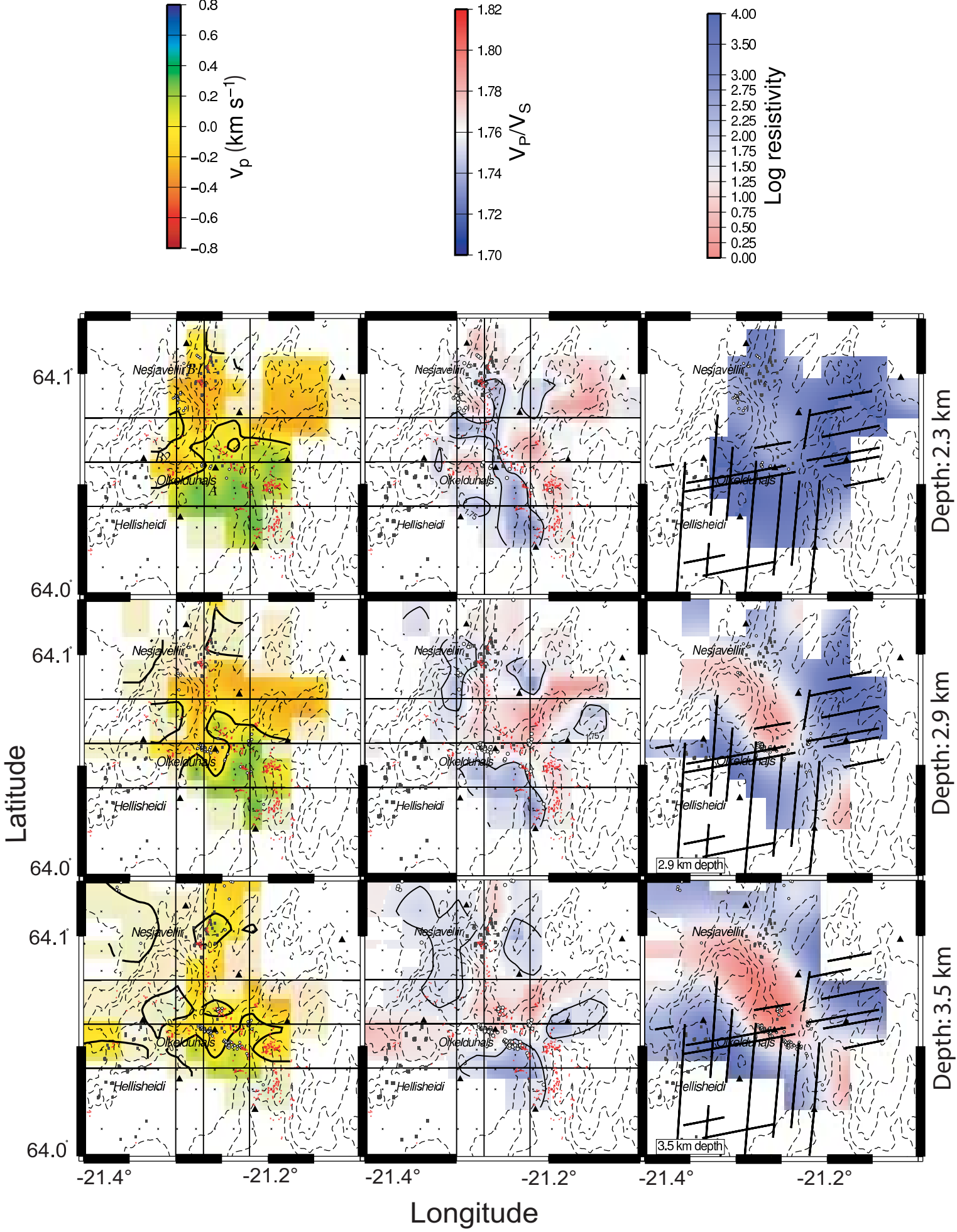
0.8
0.6
0.4
0.2
0.0
−0.2
−0.4
−0.6
−0.8
v_p (km s^{-1})
1.82
1.80
1.78
1.76
1.74
1.72
1.70
V_P/V_S
4.00
3.50
3.00
2.75
2.50
2.25
2.00
1.75
1.50
1.25
1.00
0.75
0.50
0.25
0.00
Log resistivity
Nesjavellir
Ölkelduhals
Hellisheidi
B1
B2
A
1.75
2.9 km depth
3.5 km depth
Depth: 2.3 km
Depth: 2.9 km
Depth: 3.5 km
64.1°
64.0°
-21.4°
-21.2°
Latitude
Longitude

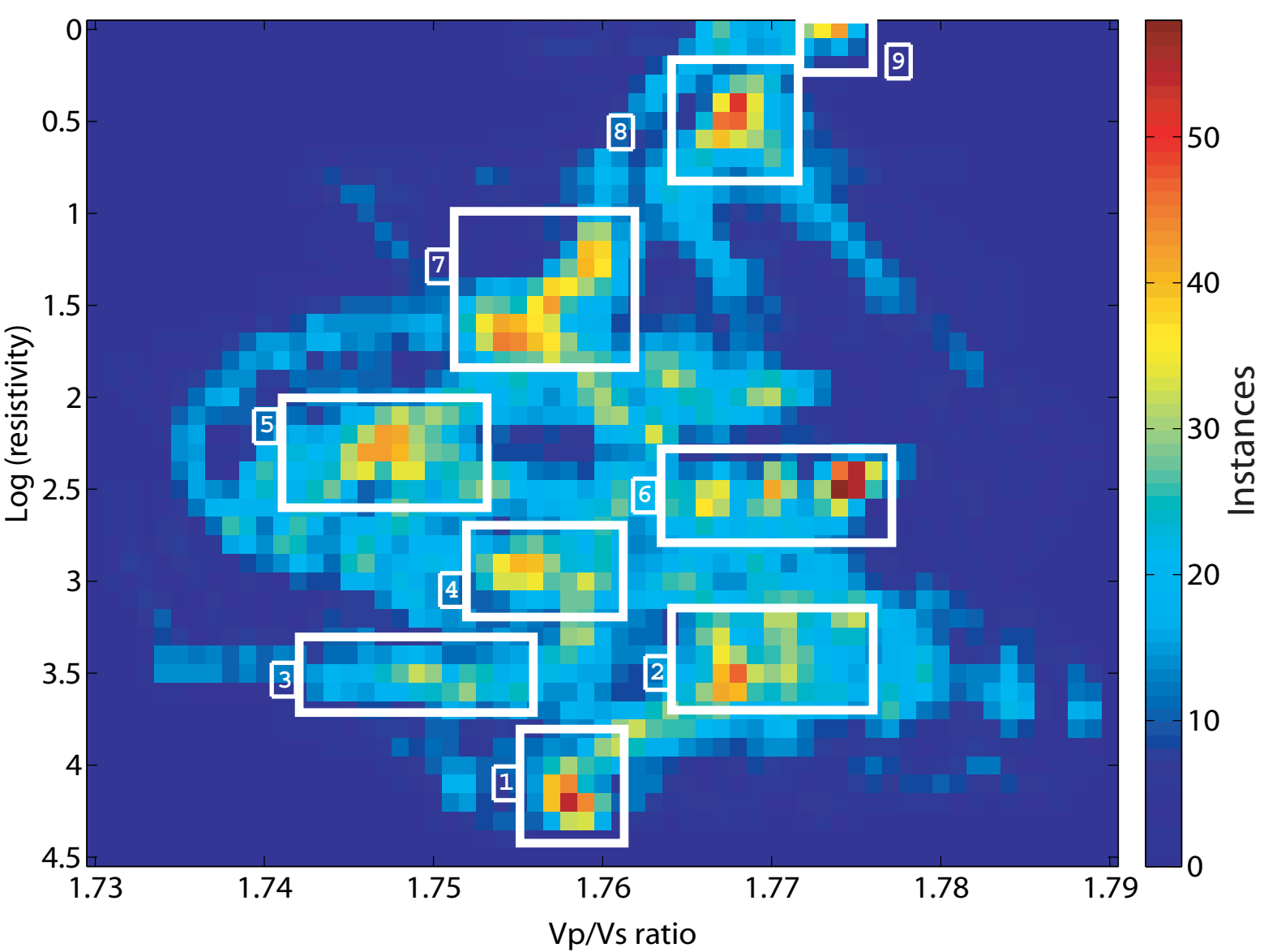
Log (resistivity)
Vp/Vs ratio
Instances
0
0.5
1
1.5
2
2.5
3
3.5
4
4.5
1.73
1.74
1.75
1.76
1.77
1.78
1.79
0
10
20
30
40
50
1
2
3
4
5
6
7
8
9

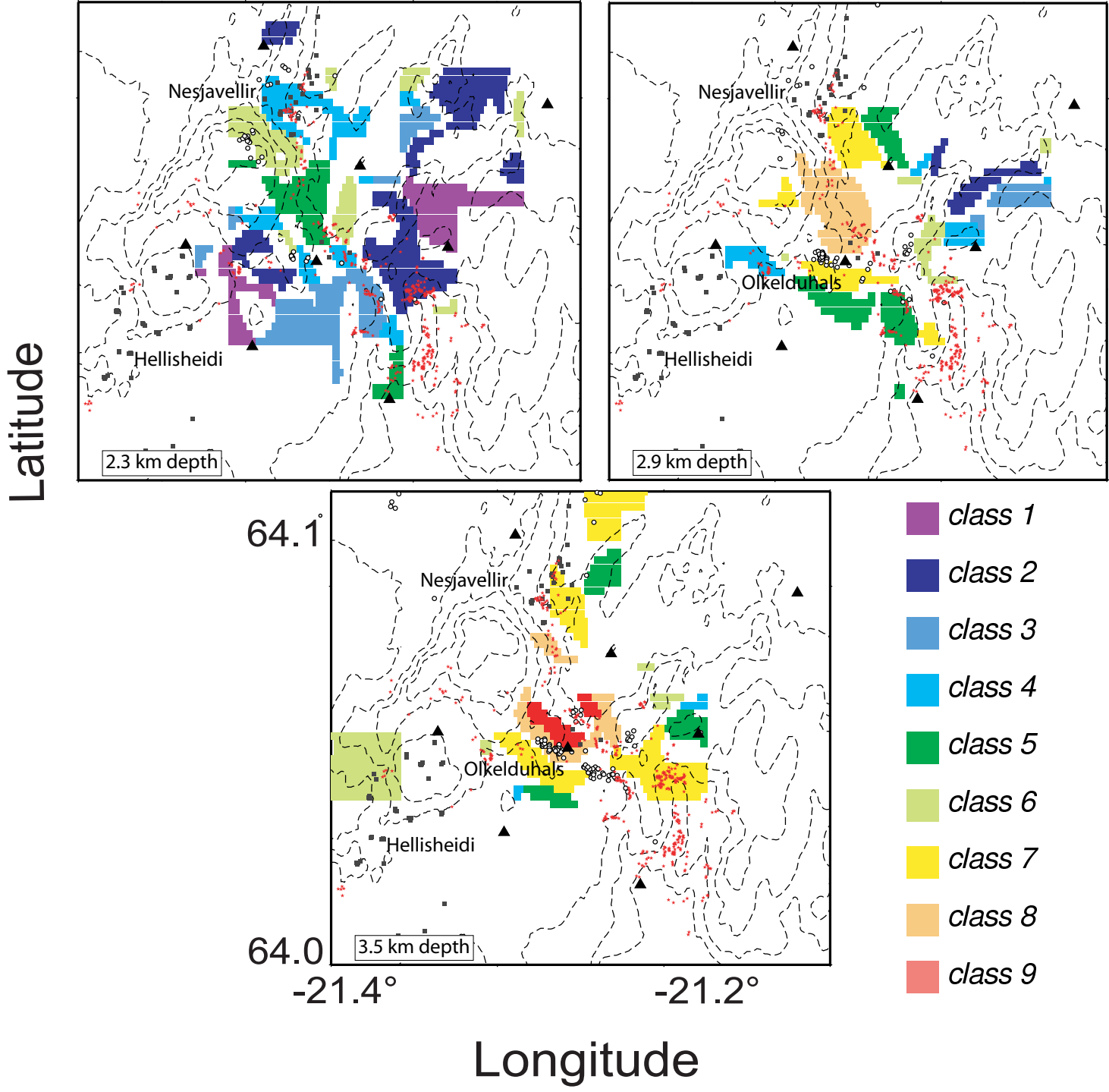
Nesjavellir
Hellisheidi
2.3 km depth
Nesjavellir
Olkelduhals
Hellisheidi
2.9 km depth
64.1°
Nesjavellir
Olkelduhals
Hellisheidi
3.5 km depth
64.0°
-21.4°
-21.2°
Latitude
Longitude
class 1
class 2
class 3
class 4
class 5
class 6
class 7
class 8
class 9

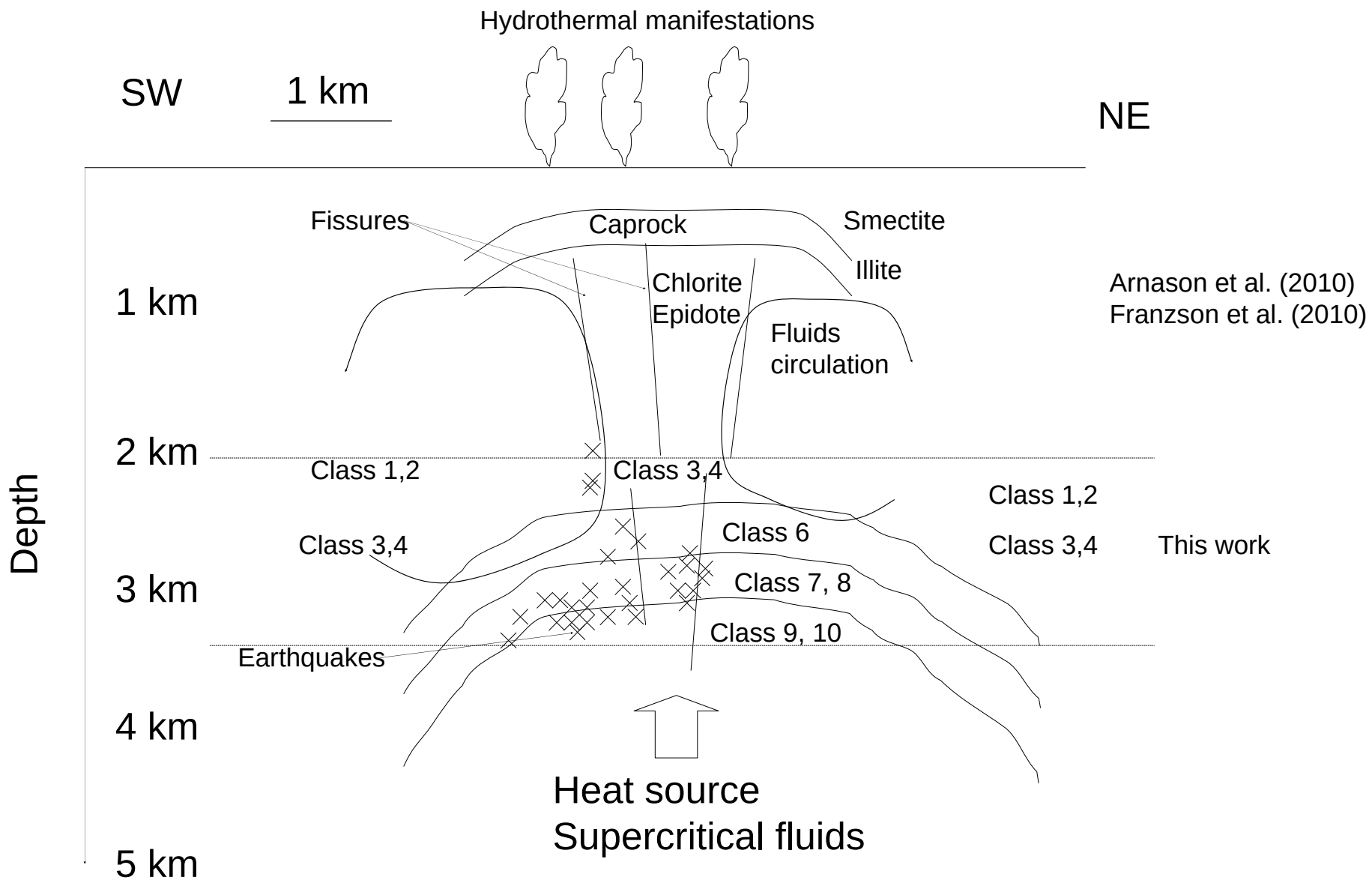
Hydrothermal manifestations
SW
1 km
NE
Depth
1 km
2 km
3 km
4 km
5 km
Fissures
Caprock
Smectite
Illite
Chlorite
Epidote
Fluids
circulation
Arnason et al. (2010)
Franzson et al. (2010)
Class 1,2
Class 3,4
Class 1,2
Class 3,4
Class 6
Class 3,4
This work
Class 7, 8
Class 9, 10
Earthquakes
Heat source
Supercritical fluids